

## GALACTIC BULGES FROM *HUBBLE SPACE TELESCOPE* NICMOS OBSERVATIONS: CENTRAL GALAXIAN OBJECTS, AND NUCLEAR PROFILE SLOPES<sup>1,2</sup>

MARC BALCELLS

Instituto de Astrofísica de Canarias, 38200 La Laguna, Tenerife, Spain

ALISTER W. GRAHAM<sup>3</sup>

Centre for Astrophysics and Supercomputing, Swinburne University of Technology, Hawthorn, VIC 3122, Australia

AND

REYNIER F. PELETIER<sup>4</sup>

Kapteyn Institute, University of Groningen, 9700 AV Groningen, Netherlands; balcells@iac.es

Received 2004 April 20; accepted 2007 May 9

### ABSTRACT

We have measured the central structural properties for a sample of S0–Sbc galaxies down to scales of  $\sim 10$  pc using *Hubble Space Telescope* NICMOS images. Central star clusters are found in 58% of our sample. Their near-infrared luminosities scale with the host bulge luminosities, as reported in 2003 by Balcells and coworkers. In terms of photometric masses, the relation is  $\mathcal{M}_{\text{PS}} = 10^{7.75 \pm 0.15} (\mathcal{M}_{\text{bul}}/10^{10} \mathcal{M}_{\odot})^{0.76 \pm 0.13}$ . Put together with recent data on bulges hosting supermassive black holes, we infer a *nonlinear* dependency of the “central massive object” mass on the host bulge mass such that  $\mathcal{M}_{\text{CMO}}/\mathcal{M}_{\odot} = 10^{7.51 \pm 0.06} (\mathcal{M}_{\text{bul}}/10^{10} \mathcal{M}_{\odot})^{0.84 \pm 0.06}$ . The linear relation presented by Ferrarese and coworkers may be biased at the low-mass end by the inclusion of the disk light from cluster lenticular galaxies. Bulge-disk decompositions reaching to the outer disk show that  $\sim 90\%$  of our galaxies possess central light excesses that can be modeled with an inner exponential and/or an unresolved source. All the extended nuclear components, with sizes of a few hundred parsecs, have disky isophotes, which suggest that they may be inner disks, rings, or bars; their colors are redder than those of the underlying bulge, arguing against a recent origin for their stellar populations. Surface brightness profiles (of the total galaxy light, and the bulge component on its own) rise inward to the resolution limit of the data, with a continuous distribution of logarithmic slopes from the low values typical of dwarf ellipticals ( $0.1 \leq \gamma \leq 0.3$ ) to the high values ( $\gamma \sim 1$ ) typical of intermediate-luminosity ellipticals; the nuclear slope bimodality reported by others is not present in our sample.

*Subject headings:* galaxies: nuclei — galaxies: spiral — galaxies: structure

*Online material:* color figures

### 1. INTRODUCTION

The *Hubble Space Telescope* (*HST*) enables the study of the inner regions of nearby bulges and ellipticals down to spatial scales of  $\sim 10$  pc, roughly 1 order of magnitude closer to the center than is feasible with typical ground-based data. These inner regions contain a small fraction of the ellipsoid mass, but they harbor the highest density regions of the galaxies and contain useful clues to their formation.

The availability of NIR array detectors in the 1990s fostered significant progress in the understanding of many aspects of bulges, including structural parameters, colors, dust content, and stellar populations, as well as the scaling of disk and bulge parameters, using ground-based imaging (e.g., Andredakis et al. 1995, hereafter APB95; de Jong 1996; Seigar & James 1998; Knapen et al. 1995; Khosroshahi et al. 2000; Graham 2001a, hereafter G01;

Möllenhoff & Heidt 2001; Graham 2001b, 2002; Eskridge et al. 2002; MacArthur et al. 2003; Castro-Rodríguez & Garzón 2003).

NIR data helped to establish that exponential profiles provide better fits to the surface brightness profiles of bulges than  $R^{1/4}$  models (Kent et al. 1991 for the Milky Way bulge; Andredakis & Sanders 1994; de Jong 1996), and soon thereafter it was demonstrated that profiles of bulges of all Hubble types admit a particularly simple fit using the Sérsic (1963; see Graham & Driver 2005) function

$$I(R) = I(0) \exp \left[ -b_n \left( \frac{R}{R_e} \right)^{1/n} \right] \quad (1)$$

(APB95; G01; Möllenhoff & Heidt 2001; MacArthur et al. 2003; see Caon et al. [1993] for the case of elliptical galaxies). In equation (1),  $R_e$  is the half-light radius of the bulge, and  $b_n \approx 1.9992n - 0.3271$ . The Sérsic index  $n$ , which measures the curvature of the surface brightness profile, scales with bulge-to-disk luminosity ratio ( $B/D$ ) and with bulge luminosity. The Sérsic index also provides a concentration parameter (Trujillo et al. 2001) that strongly correlates with the velocity dispersion and central supermassive black hole mass (Graham et al. 2001a, 2001b); hence, it is linked to global physical parameters of the spheroid. Numerical simulations also suggest that bulges have a range of profile shapes. Aguerri et al. (2001) showed that the accretion of dense satellites

<sup>1</sup> Based on observations made with the NASA/ESA *Hubble Space Telescope*, obtained at the Space Telescope Science Institute, which is operated by the Association of Universities for Research in Astronomy, Inc., under NASA contract NAS 5-26555.

<sup>2</sup> Based on observations made with the Isaac Newton Telescope operated on the island of La Palma by the Isaac Newton Group of Telescopes in the Spanish Observatorio del Roque de los Muchachos of the Instituto de Astrofísica de Canarias.

<sup>3</sup> Also at Instituto de Astrofísica de Canarias, 38200 La Laguna, Tenerife, Spain.

<sup>4</sup> Also at School of Physics and Astronomy, University of Nottingham, NG7 2RD, UK.

onto disk-bulge-halo galaxies yields a growth of both the Sérsic index and  $B/D$ , hinting that  $n$  may be linked to the accretion history and to the growth of bulges.  $\Lambda$ CDM cosmological simulations of galaxy formation yield bulge-disk structures in which the bulge profile shape ranges from exponential to  $R^{1/4}$  (Scannapieco & Tissera 2003; Sommer-Larsen et al. 2003).

The results given above, derived from ground-based data, bear the question of whether the inner regions to which the *HST* gives access also follow the Sérsic function. Our picture of elliptical galaxy nuclei had to be revised in several ways after the *HST* imaging campaigns. Giant ellipticals often show a rather sudden inward flattening of their surface brightness profiles, confirming the result from ground-based data that some ellipticals have “cores” (Kormendy 1985), while intermediate-luminosity ellipticals ( $-18 \leq M_B \leq -20.5$ ) do not show cores; their profiles approach power laws throughout the inner regions (“power-law” galaxies; see Faber et al. 1997, hereafter F97; Rest et al. 2001, hereafter R01). Inner profile slopes decrease toward fainter luminosities, and, for dwarf ellipticals, approach the slopes seen in the nuclei of giant, core galaxies, although dwarfs do not show profile discontinuities, i.e., do not show cores (Graham & Guzmán 2003; Ferrarese et al. 2006, hereafter F06). Many cores of ellipticals and S0s are dusty, and a fraction of them harbor central unresolved sources at *HST* resolution (Lauer et al. 1995, hereafter L95; Phillips et al. 1996; Carollo et al. 1997; Ravindranath et al. 2001; Stiavelli et al. 2001). Inasmuch as bulges share global similarities with ellipticals when studied from the ground, we inquire whether bulges show cores or nuclear sources.

Bulges of disk galaxies have been targeted less often than ellipticals by the *HST*. Peletier et al. (1999, hereafter Paper I) analyzed a sample of 19 field S0–Sbc galaxies using Wide Field and Planetary Camera 2 (WFPC2) F450W and F814W, and NICMOS F160W images, with the goal of obtaining bulge stellar population diagnostics. The combination of blue and NIR colors allowed them to put tight limits on the ages of bulge populations. Ages of S0 to Sbc bulges were found to be comparable to those of ellipticals in the Coma cluster, with a small age spread,  $< 2$  Gyr (Sbc bulges showed colors corresponding to younger ages). Nuclei were found to be dusty, with  $A_V = 0.6$ – $1.0$  mag.

Carollo and collaborators surveyed mid- to late-type bulges using WFPC2 and NICMOS (e.g., Carollo 1999; Carollo & Stiavelli 1998; Carollo et al. 1998, 2001, 2002; Seigar et al. 2002). These authors focused on bulge structure. They provided fits using the  $R^{1/4}$ , exponential, and Nuker models, and proposed a structural classification of bulges into “ $R^{1/4}$  classical” and “exponential.” Carollo et al. (2002) found nuclear resolved components (NCs) in the centers of 60% of the exponential bulges. In their view,  $R^{1/4}$  and exponential bulges show, respectively, high and low nuclear profile slopes, a structural difference that would trace different formation histories.

Whether bulges come in two families with distinct structural properties has implications for formation mechanisms of bulges. Several models have been proposed (see Wyse et al. 1997; Bouwens et al. 1999; Kormendy & Kennicutt 2004): early collapse (Renzini 1999; Zoccali et al. 2003), mergers prior to disk formation (Kauffmann et al. 1996), satellite accretion (Pfenniger 1993; Aguerrí et al. 2001), and disk instabilities (Pfenniger & Norman 1990; Zhang 1999). Bulges with  $R^{1/4}$  structure fit in the early collapse or merger scenarios, while exponential bulges are destroyed by mergers (Aguerrí et al. 2001) and may instead be expected from disk instabilities (Combes et al. 1990). Edge-on, peanut-shaped bulges are known to have bar dynamics and are therefore also expected to form from disk instabilities (Kuijken

& Merrifield 1995; Bureau & Freeman 1999). The existence of two classes of bulges is commonly understood as evidence that massive bulges come from mergers while less massive bulges grow as a result of disk instabilities (see, e.g., Athanassoula 2005).

In this paper we analyze the structural properties of bulges of early- to intermediate-type galaxies at *HST* resolution using the S0–Sbc sample presented in Paper I. We address profile shapes, nuclear sources, nuclear slopes, and central massive black hole mass estimates. Given the ability of the Sérsic model to describe the profiles of spheroids at ground-based resolution, we use the Sérsic model as our starting point and inquire whether the increased spatial resolution of the *HST* contributes to support or to modify the ground-based picture. We perform a bulge-disk decomposition of the surface brightness profiles using combined *HST*+ground-based profiles that sample the galaxy light distribution from the nucleus to the disk-dominated region. Ignoring this step would bring up two problems: the unmodeled disk contribution to the inner profile would bias the bulge nuclear parameters; and we would not be able to derive basic bulge parameters such as the total luminosity and the effective radius, as the *HST* images do not cover the entire bulge at the distances of our target galaxies.

We avoid using the  $R^{1/4}$  or exponential models; rather, we focus on Sérsic fits to the bulge profiles to test if the profile shape dichotomy appears when it is not forced. Our first results on bulge profile shapes using *HST* data were presented in Balcells et al. (2003, hereafter Paper II). In that paper we showed that  $R^{1/4}$  bulge profiles are exceedingly rare. In this and a companion paper (Balcells et al. 2007, hereafter Paper IV) we perform a comprehensive analysis of those profiles. We show that inner surface brightness profiles show excesses, over the best-fit bulge Sérsic model, which can be successfully modeled by adding central unresolved sources and/or inner exponential components to the fitting function (§ 3). Section 4 provides details on the estimation of parameter errors through fits to simulated profiles. The subsequent sections analyze the properties of the nuclear excess light. Section 5.1 shows that the galaxies with extended nuclear components closely match those with nuclear disky isophotes, which suggests that the excess light in the surface brightness profiles comes from flattened components such as disks, rings, or inner bars. Section 5.2 derives luminosities and masses for the unresolved nuclear sources and addresses the compact massive object (CMO) paradigm, i.e., that nuclear star clusters are the low-mass extension to central supermassive black holes. In § 5.3 we relate the point sources to black hole mass estimates from the bulge velocity dispersions. Finally, in § 5.4 we present and discuss the nuclear surface brightness profile slopes and compare them to those of ellipticals, bulges, and dwarf ellipticals. In Paper IV we discuss global bulge and disk scaling relations as inferred from the profile decompositions. A Hubble constant of  $H_0 = 75 \text{ km s}^{-1} \text{ Mpc}^{-1}$  is used throughout.

## 2. GALAXY SAMPLE AND DATA

We have analyzed 19 galaxies from the Balcells & Peletier (1994, hereafter BP94) diameter-limited sample of inclined, early- to intermediate-type disk galaxies. The BP94 sample was selected from the Uppsala General Catalog of Galaxies (UGC; Nilson 1973) to include all disk galaxies of types S0 to Sbc, listed as unbarred in the UGC, with blue diameters greater than  $2'$ , inclinations above  $50^\circ$  (i.e., mid- to high inclination), and apparent blue magnitudes brighter than 14.0 mag, within given limits of equatorial and Galactic coordinates. Upon inspection, some cases

TABLE 1  
 GALAXY SAMPLE

NGC (1)	$T$ (2)	$D$ (Mpc) (3)	Scale (kpc arcsec $^{-1}$ ) (4)	$K$ (mag) (5)	$M_K$ (mag) (6)	$M_R$ (mag) (7)	$\sigma_0$ (km s $^{-1}$ ) (8)	$\epsilon_{\text{disk}}$ (9)
5326.....	1	34.3	0.166	8.99 $\pm$ 0.12	-23.72 $\pm$ 0.13	-21.28	164 $\pm$ 6	0.55
5389.....	0	26.2	0.127	8.57 $\pm$ 0.06	-23.55 $\pm$ 0.08	-20.44	114 $\pm$ 6	0.75
5422.....	-2	25.3	0.123	8.88 $\pm$ 0.05	-23.16 $\pm$ 0.08	-21.08	160 $\pm$ 6	0.80
5443.....	3	27.2	0.132	9.06 $\pm$ 0.23	-23.13 $\pm$ 0.24	-20.65	76 $\pm$ 8	0.72
5475.....	1	24.5	0.119	9.30 $\pm$ 0.03	-22.67 $\pm$ 0.07	-20.10	91 $\pm$ 6	0.71
5577.....	4	19.6	0.095	9.53 $\pm$ 0.08	-21.96 $\pm$ 0.11	-19.63	... $\pm$ ...	0.72
5587.....	0	31.0	0.150	9.61 $\pm$ 0.09	-22.88 $\pm$ 0.10	-20.19	93 $\pm$ 8	0.70
5689.....	0	30.3	0.147	8.50 $\pm$ 0.28	-23.94 $\pm$ 0.28	-21.41	143 $\pm$ 6	0.75
5707.....	2	31.1	0.151	9.31 $\pm$ 0.08	-23.18 $\pm$ 0.09	-20.55	141 $\pm$ 6	0.75
5719.....	2	23.1	0.112	8.40 $\pm$ 0.09	-23.44 $\pm$ 0.11	-20.72	108 $\pm$ 6	0.68
5746.....	3	22.9	0.111	6.88 $\pm$ 0.04	-24.95 $\pm$ 0.07	-21.80	139 $\pm$ 8	0.83
5838.....	-3	18.3	0.089	7.72 $\pm$ 0.07	-23.63 $\pm$ 0.11	-21.01	255 $\pm$ 6	0.63
5854.....	-1	23.3	0.113	8.63 $\pm$ 0.17	-23.24 $\pm$ 0.18	-20.55	97 $\pm$ 6	0.70
5879.....	4	13.8	0.067	8.79 $\pm$ 0.22	-21.92 $\pm$ 0.24	-19.42	58 $\pm$ 8	0.70
5965.....	3	47.6	0.231	8.61 $\pm$ 0.20	-24.82 $\pm$ 0.20	-22.04	162 $\pm$ 8	0.83
6010.....	0	26.0	0.126	8.82 $\pm$ 0.34	-23.31 $\pm$ 0.34	-20.69	144 $\pm$ 6	0.77
6504.....	2	61.9	0.300	9.21 $\pm$ 0.07	-24.81 $\pm$ 0.07	-23.69	185 $\pm$ 6	0.80
7457.....	-3	13.7	0.066	8.70 $\pm$ 0.16	-22.00 $\pm$ 0.19	-20.03	56 $\pm$ 6	0.48
7537.....	4	35.3	0.171	9.68 $\pm$ 0.20	-23.11 $\pm$ 0.20	-20.49	42 $\pm$ 9	0.66

NOTES.—Col. (1): Galaxy NGC number. Col. (2): Morphological type index from RC3. Col. (3): Galaxy distance, computed from the Galactic standard-of-rest recession velocities listed in RC3, assuming  $H_0 = 75 \text{ km s}^{-1} \text{ Mpc}^{-1}$ . Col. (4): Spatial scale at the galaxy distance. Col. (5): Galaxy  $K$ -band apparent magnitude, from our photometry (§ 2). Col. (6): Galaxy  $K$ -band absolute magnitude, using the distances in col. (2), with Galactic extinction, cosmological correction, and  $K$ -correction. Col. (7): Galaxy  $R$ -band absolute magnitude, from BP94, for the assumed cosmology. Col. (8): Aperture-corrected central velocity dispersion, from Falcón-Barroso et al. (2002). Col. (9): Disk ellipticity derived from  $K$ -band images, from APB95.

were excluded due to being obviously barred, interacting, or very dusty, leaving 30 galaxies that were analyzed in BP94, APB95, and Peletier & Balcells (1996, 1997). The present subsample comprises 19 galaxies of types S0 to Sbc that were imaged with *HST* (NICMOS F160W [camera 2] and WFPC2 F450W and F814W; Paper I). The subsample was selected to provide representative examples of each Hubble type and to exclude cases where dust obscured the nuclei. Due to their high inclinations, some of the galaxies may harbor bars that go undetected in the images; bars may be suspected from the peanut-shaped isophotes of some of the bulges (e.g., Kuijken & Merrifield 1995). None of the galaxies have a Seyfert or a starburst nucleus.

The sample has been extensively studied by us in previous papers. Nuclear colors at *HST* resolution and bulge ages have been presented in Paper I, where postage-stamp images of the *HST* data for the 19 galaxies studied here may be found. Peletier & Balcells (1997) published  $K$ -band surface brightness profiles and isophotal parameters from ellipse fits to wider field-of-view United Kingdom Infrared Telescope (UKIRT) images. Central stellar velocity dispersions and a fundamental plane analysis are given in Falcón-Barroso et al. (2002). Minor-axis kinematic profiles are presented in Falcón-Barroso et al. (2003).

The inclined viewing angle for this sample presents advantages and disadvantages for a structural study of the nuclear properties of disk galaxies. The main drawback is extinction, which can completely hamper detection of nuclear structures at visible wavelengths. Fortunately, extinction is smaller at NIR wavelengths. Paper I concluded that extinction for this sample is on average  $A_H = 0.1\text{--}0.2$  mag in the nucleus, and much lower farther out. Problems related to extinction should therefore be minor for the study presented here. The main advantage of working with an inclined sample is that isophotes provide information on the flatness of each galaxian component, and hence they guide in the identification of these components.

Basic properties of the sample are given in Table 1, where we list distances, spatial scales,  $K$ - and  $R$ -band absolute magnitudes, central velocity dispersions, and disk ellipticities. Distances are derived from recession velocities relative to the Galactic standard of rest, from de Vaucouleurs et al. (1991, hereafter RC3). We present new  $K$ -band apparent and absolute magnitudes for the program galaxies. The photometry we had published in APB95 is about 0.5 mag brighter than that from the Two Micron All Sky Survey (2MASS); new ellipse fits to the APB95 images yield total  $K$ -band apparent magnitudes that closely match 2MASS total magnitudes (mean difference of 0.00 mag; rms of 0.21 mag). The coincidence of our photometry and that of 2MASS makes us believe that the present photometric zero points are more accurate than those of APB95. Therefore, we adopt the new apparent magnitudes in this paper, except for NGC 5746 and 5965, which overflow our frames, and for NGC 5879, whose frame suffers from bad-sky planarity. For those three galaxies we adopt the total absolute magnitudes from the NASA/IPAC Extragalactic Database (NED). Adopted apparent magnitudes are listed in Table 1. Absolute  $K$ -band magnitudes are corrected for Galactic extinction, cosmological dimming, and  $K$ -correction. Errors in the  $K$ -band absolute magnitude include the photometric error and a distance modulus error that assumes a flat 50 km s $^{-1}$  recession velocity error. We use the disk ellipticities from APB95, which have been derived on  $K$ -band images; these ellipticities show minimal differences, of at most 0.05, with respect to the  $R$ -band values given in BP94.

Details of the *HST* observations and the reduction of the *HST* data are given in Paper I. Here we derive elliptically averaged surface brightness profiles and isophotal shapes from the *HST* NICMOS F160W images ( $19'' \times 19''$ ;  $0.075''$  pixel $^{-1}$ ), from  $0.03''$  (1/2 pixel size) to typically  $10''$ , using the GALPHOT package (Jørgensen et al. 1992). We keep the centers fixed at the galaxy luminosity peak and let the ellipticity and position angle of the isophotes vary.

To extend the surface brightness profiles to large radii, we use the elliptically averaged  $K$ -band surface brightness profiles derived from UKIRT IRCAM3 images (mosaics of  $75'' \times 75''$  frames;  $0.291'' \text{ pixel}^{-1}$ ) published by Peletier & Balcells (1997), which we transform to the  $H$  band by approximating the  $H - K$  profiles with the transformation

$$H - K = 0.111(I - K) - 0.0339 \quad (2)$$

derived from the GISSEL96 models of Bruzual & Charlot (see Leitherer et al. 1996) using  $I - K$  profiles from Peletier & Balcells (1997).

The  $HST$  and ground-based (GB) profiles have matching slopes in the range  $3'' \leq r \leq 8''$  and show zero-point offsets that are always below 0.1 mag. We correct these by applying an offset to the GB profiles, which overall have less photometric accuracy. The process described here is the same that was employed in Paper I to derive color profiles for bulges at  $HST$  resolution. The match of GB to  $HST$  profiles is extremely good, as can be seen in the residual profiles presented below (see the Appendix; Fig. 8). The resulting geometric-mean-axis profiles were used in Paper II for the analysis of the Sérsic shape index  $n$ .

### 3. PROFILE DECOMPOSITION

The decomposition of the surface brightness profiles was described in Paper II. Briefly, the combined  $HST$ +GB profiles were fitted with a PSF-convolved Sérsic plus exponential law using the code described in G01, modified to use a Moffat point-spread function (PSF;  $\beta = 6.9$ ). The Moffat FWHM =  $0.131''$  used here is slightly narrower than that used in Paper II. This has two consequences: first, the light in the NICMOS PSF wings needs to be accounted for with a suitable correction (§ 4); and second, more nuclear components appear as resolved in the present fits than they did in Paper II. Fitting proceeded by  $\chi^2$  minimization, allowing all five free parameters (disk  $\mu_0$  and  $h$ ; bulge  $\mu_e$ ,  $R_e$ , and  $n$ ) to vary. Convergence was generally straightforward, except for NGC 5326 and NGC 5854, where we fixed the disk parameters by eye. In a few other cases, a few outer low signal-to-noise ratio (S/N) points were excluded to prevent downward deviations from distorting the fit in the main part of the disk (see Fig. 1).

We found that pure Sérsic+exponential fits to the entire radial range of the profiles provide an inaccurate description of the data: the residuals from the fits show a strong wave pattern with an obvious central positive residual. An example of this feature is shown in Figure 1 of Paper II. As a consequence, the bulge and disk fitted parameters are highly sensitive to any inner radius cutoff imposed on the fitting range. Such fits yield uncertain values for the bulge Sérsic index  $n$ , the total bulge luminosities, and the bulge-to-disk ratios. Fits excluding the inner  $\sim 0.5'' - 1.0''$  in radius (a common approach for deriving bulge parameters in the presence of nuclear components; e.g., Carollo et al. 1998; Stiavelli et al. 2001) show strong central residuals (see Fig. 8, *second rows*). These indicate that our galaxy surface brightness profiles cannot be modeled with just the sum of a Sérsic bulge and an exponential disk. For 14 out of 19 galaxies, we find an excess of central light above the Sérsic bulge; 2 galaxies show central depressions, while 3 follow the Sérsic profile reasonably well over the entire radial range. These numbers do not substantially vary when modifying the inner radial cutoff.

The failure of pure Sérsic+exponential fits suggests that many of our program galaxies harbor nuclear components. The detection of central excesses has previously been reported for bulges, dwarf ellipticals, and intermediate-luminosity ellipticals (Aaronson 1978;

Binggeli et al. 1984; Caldwell & Bothun 1987; Phillips et al. 1996; Carollo et al. 1997; R01; Ravindranath et al. 2001). Excluding the central  $\sim 1''$  has been a common strategy to cope with these central components, which also avoids the problems with central dust extinction, e.g., the Stiavelli et al. (2001) fits to  $HST$ -based dwarf elliptical surface brightness profiles, or the  $R^{1/4}$  or exponential fits to bulge surface brightness profiles by Carollo et al. (1998). In our case, outside  $1''$ , the pure Sérsic+exponential bulge-disk fits are quite satisfactory (see Fig. 8), suggesting that the Sérsic model provides a good approximation to the large-scale brightness profiles of bulges.

We therefore assume that the Sérsic model describes the “bulge,” taken as the spheroidal component residing in the center of the disk galaxy, and that any central excess above the Sérsic profile is due to additional photometric components. To implement our approach, we run the fitting program with additional central components. We tested central point sources (PSs), central exponential disks, a combination of both, and central Gaussians of free width. In all cases, the models were convolved with the Moffat PSF prior to fitting. For each galaxy, all fits were inspected, and we selected the fits that, with a minimum number of added components, resulted in residual profiles without structures such as the wave pattern described above. In all cases, we adopted the extra component when the root mean square (rms) of the residuals improved by over 10%, and we discarded it when the rms improved by less than 10%. From a formal point of view, this approach is justified given that, with typically 90 independent data points, adding a point source to the five-parameter Sérsic+exponential fit would trivially yield an rms decrease of  $< 2.8\%$ ; including an additional nuclear exponential to the above solution would trivially improve the rms of that solution by 4.0%; and, an rms trivial improvement of 10% would be expected only after adding 18 constraints to the fit. Moreover, the adequacy of the employed model is ascertained through examination of the shape of the residual profile. Fits with residual profiles that were featureless were adopted without testing more complex models, as the rms cannot be improved by modifying the functional form of the fitted model in those cases. Residual profiles for the adopted solutions have  $0.02 \text{ mag} \leq \text{rms} \leq 0.1 \text{ mag}$ .

Hence, our approach has two steps: first, a  $\chi^2$  minimization of five different models, namely, pure Sérsic+exponential, Sérsic+exponential+Moffat, Sérsic+exponential+inner exponential, Sérsic+exponential+Moffat+inner exponential, and Sérsic+exponential+Gaussian; and second, a selection of the best of these models, applying Occam’s razor to choose the simplest model that describes the data. Our solutions describe the surface brightness profiles to a high degree of accuracy, although we generally cannot guarantee to have obtained unique solutions. Parameter uncertainties are discussed in § 4.

Figure 1 shows the profiles, the best-fit models, and the residual profiles from the fits for the 19 galaxies. Parameters for the fits are given in Table 2. The largest structures in the residual profiles occur in the region of the disk and are due to spiral arms and other disk features. In the bulge-dominated region, the small oscillation around  $0.2''$  arises from the cross-pattern in the NICMOS PSF wings and deviations from the assumed Moffat model (§ 4).

Internal extinction is obviously an issue at the galaxy centers. Fortunately, our use of NIR imaging data strongly alleviates the problem. Paper I shows that  $A_{V,\text{center}} = 0.6 - 1.0 \text{ mag}$  on average for this sample, which corresponds to  $A_H$  between 0.1 and 0.2 mag. Extinction is highly concentrated in the inner  $\sim 100 \text{ pc}$  and hence is probably local rather than due to intervening disk dust. This extinction must vary from galaxy to galaxy and can be estimated from the excess of central  $I - H$  color with respect to a typical bulge stellar population. The resulting values are so small that we

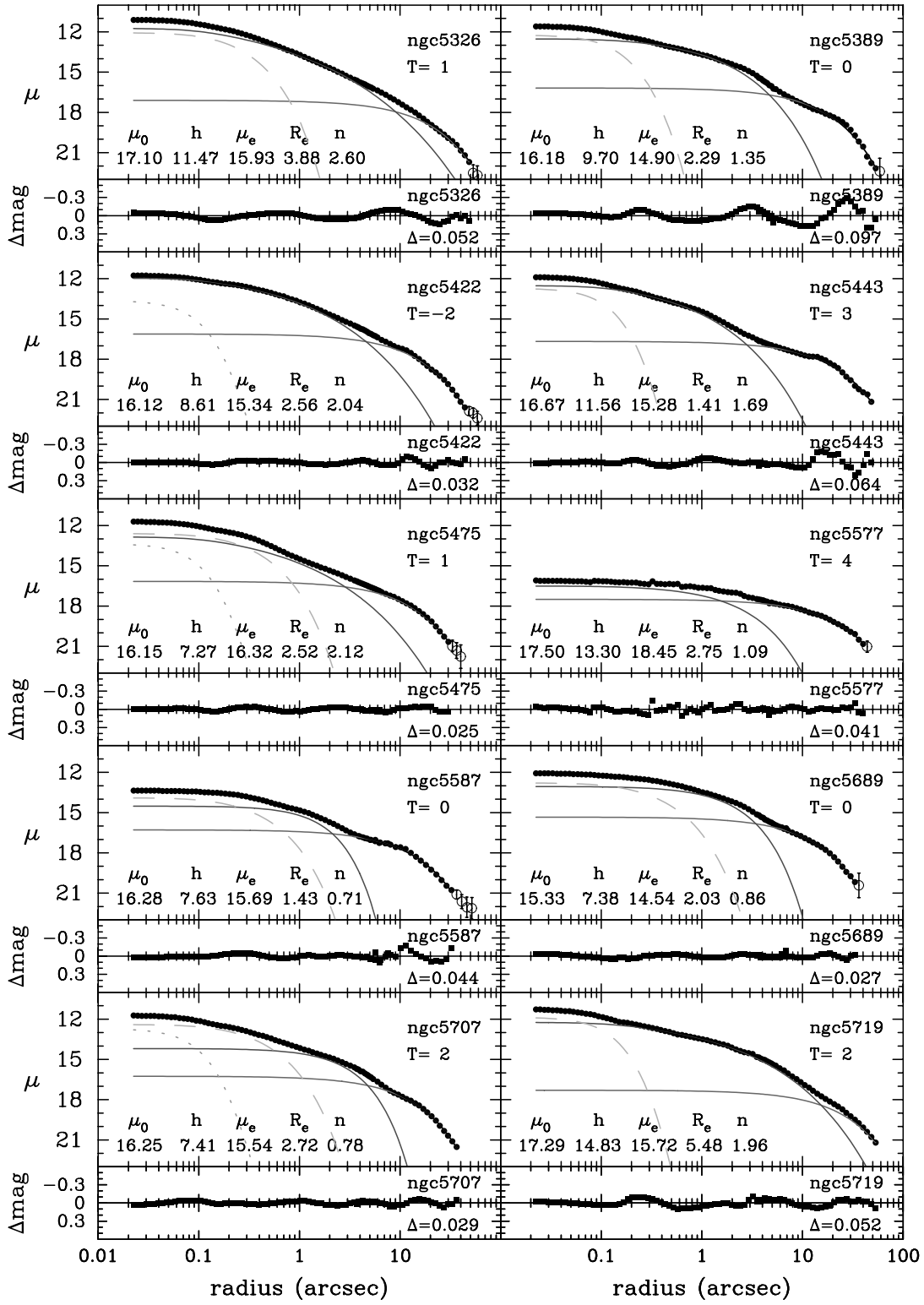


FIG. 1.—*H*-band combined *HST* plus ground-based surface brightness profiles for the 19 galaxies, and best-fit models. The abscissa is the geometric mean radius in arcseconds,  $r \equiv a\sqrt{(1-\epsilon)}$ , where  $a$  is the major axis, and  $\epsilon$  is the ellipticity. *Filled circles*: Fitted data points. *Open circles*: Outer points excluded from the fit. *Solid lines*: Seeing-convolved Sérsic bulge and exponential outer disk models. *Dotted lines*: Seeing-convolved inner point sources. *Dashed lines*: Inner exponential components. Given in each panel are the best-fit outer disk parameters (central surface brightness  $\mu_0$ , disk scale length  $h$ ) and bulge parameters (effective surface brightness  $\mu_e$ , effective radius  $R_e$ , and Sérsic index  $n$ ). Parameters for the inner components are given in Table 2. Below each profile is the profile residual (data minus model);  $\Delta$  gives the rms residual from the fit, in magnitudes. [See the electronic edition of the *Journal* for a color version of this figure.]

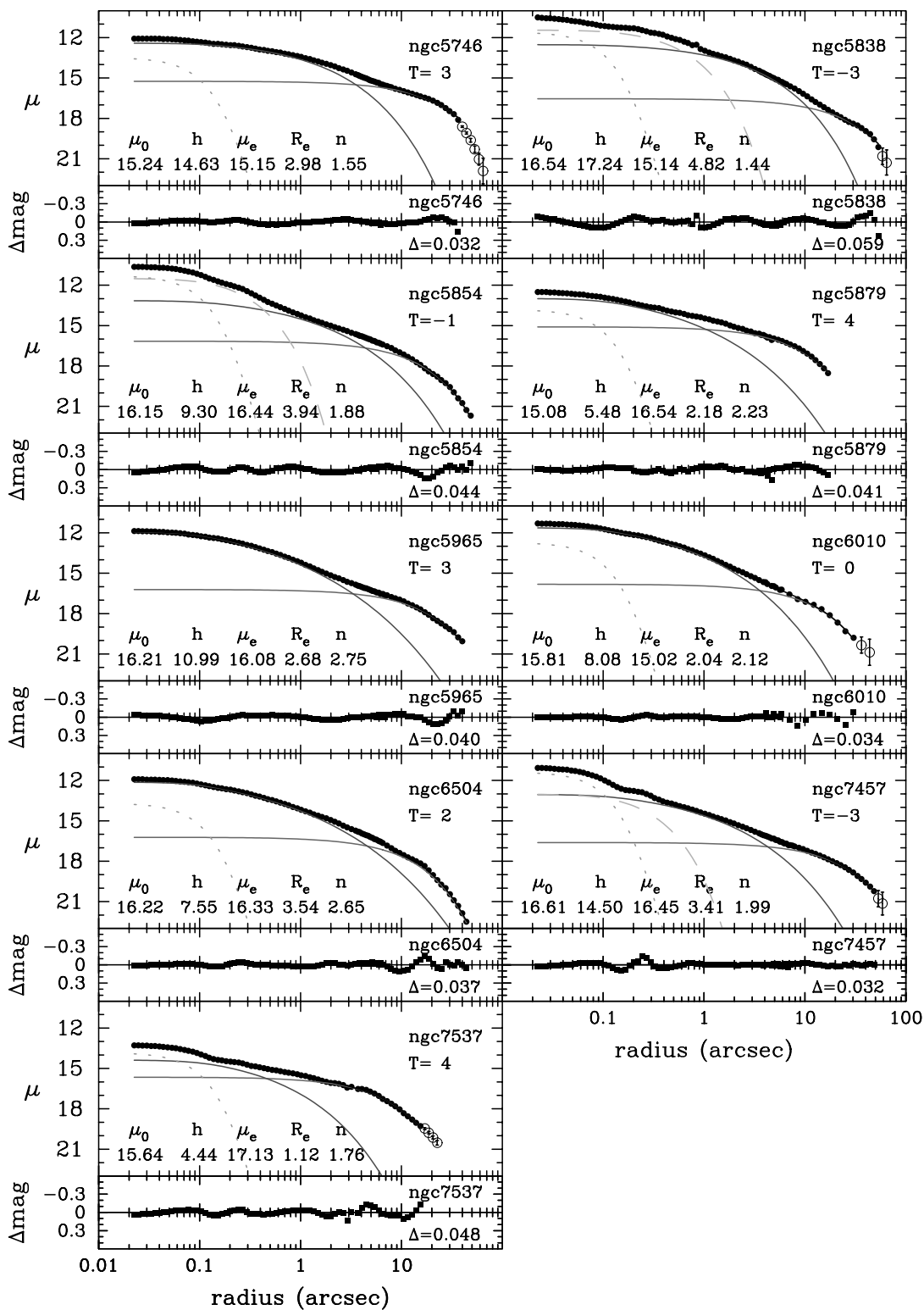


FIG. 1—Continued

do not apply extinction corrections to our photometry. The lack of such correction does not affect any of the conclusions of the paper.

#### 4. PARAMETER UNCERTAINTIES

Simulations with synthetic profiles were carried out to estimate errors in parameter recovery. The simulation work addresses two main questions. First is parameter coupling, especially between bulge and nuclear components; e.g., a profile consisting of a high-

$n$  Sérsic and an outer exponential might be reproduced by the fitting program as a nuclear component, a lower- $n$  Sérsic, and an outer exponential. A second important issue is whether our choice of a Moffat PSF is adequate. The TinyTim PSF for our NICMOS images comprises a central peak surrounded by a secondary maximum at about  $0.23''$ . An analytical PSF such as the Moffat function is particularly convenient for one-dimensional profile fitting but may affect the parameters derived for nuclear sources, and the

TABLE 2  
BEST-FIT PARAMETERS FOR THE DISK, BULGE, AND NUCLEAR COMPONENTS

NGC (1)	$\mu_0$ (2)	$h$ (3)	$\mu_e$ (4)	$R_e$ (5)	$n$ (6)	$B/D$ (7)	$H_{PS}$ (8)	$H_{E2}$ (9)	$\mu_{0,2}$ (10)	$h_2$ (11)	Fit Type (12)
5326.....	17.10	11.47	15.93	3.88	2.60	0.99	...	13.64	11.55	0.15	ese
5389.....	16.18	9.70	14.90	2.29	1.35	0.39	...	15.19	11.04	0.06	ese
5422.....	16.11	8.61	15.34	2.56	2.04	0.47	17.79	...	...	...	pse
5443.....	16.67	11.56	15.28	1.41	1.69	0.13	...	16.34	10.57	0.03	ese
5475.....	16.15	7.27	16.32	2.52	2.12	0.27	17.51	13.50	12.24	0.22	pese
5577.....	17.50	13.30	18.45	2.75	1.09	0.04	...	...	...	...	se
5587.....	16.28	7.63	15.69	1.43	0.71	0.10	...	14.49	13.59	0.26	ese
5689.....	15.33	7.38	14.54	2.03	0.86	0.28	...	13.39	12.48	0.26	ese
5707.....	16.25	7.41	15.53	2.72	0.78	0.45	16.87	12.95	12.10	0.27	pese
5719.....	17.30	14.83	15.72	5.48	1.96	1.50	...	15.34	10.06	0.04	ese
5746.....	15.24	14.63	15.15	2.98	1.55	0.10	17.65	...	...	...	pse
5838.....	16.54	17.24	15.14	4.82	1.44	0.63	15.76	11.42	11.21	0.36	pese
5854.....	16.15	9.30	16.44	3.94	1.88	0.35	15.45	12.96	11.02	0.16	pese
5879.....	15.08	5.48	16.54	2.18	2.23	0.11	17.97	...	...	...	pse
5965.....	16.21	10.99	16.08	2.68	2.75	0.20	...	...	...	...	se
6010.....	15.81	8.08	15.02	2.04	2.12	0.36	16.89	...	...	...	pse
6504.....	16.22	7.55	16.32	3.54	2.65	0.59	17.85	...	...	...	pse
7457.....	16.61	14.50	16.45	3.41	1.99	0.17	15.53	14.55	12.53	0.16	pese
7537.....	15.64	4.44	17.14	1.12	1.76	0.04	17.99	...	...	...	pse

NOTES.—This table lists output parameters from the surface brightness profile fitting code, prior to applying the corrections described in § 4. All surface brightnesses are given in  $H$ -band mag arcsec $^{-2}$  and are not corrected to face-on view. All scale lengths, in arcseconds, refer to the geometric mean axis  $(ab)^{1/2}$  of each measured ellipse. Col. (1): Galaxy NGC number. Col. (2): Extrapolated disk central surface brightness. Col. (3): Disk scale length. Col. (4): Bulge effective surface brightness. Col. (5): Bulge effective radius. Col. (6): Bulge Sérsic index. Col. (7): Luminosity ratio between bulge and main disk, from best-fit parameters ( $H$  band). Col. (8):  $H$ -band magnitude of the central unresolved source, from best-fit parameters ( $H$  band). Col. (9):  $H$ -band magnitude of the nuclear exponential component, from best-fit parameters ( $H$  band). Col. (10): Extrapolated central surface brightness of the nuclear exponential. Col. (11): Scale length of the nuclear exponential. Col. (12) Fit type code—se: Sérsic bulge and exponential outer disk; pse: se plus a nuclear point source; ese: se plus an inner exponential component; pese: se plus a nuclear point source and a nuclear exponential component.

light in the secondary maximum may masquerade as an extended component.

For the simulations, synthetic images were generated with IRAF's `mkobjects` task, comprising a Sérsic component and an outer exponential component, with and without nuclear components. Nuclear components were either a point source, a Gaussian, or an inner exponential. The sampled range for the parameters was bigger than that displayed by our target galaxies. The images were convolved with TinyTim PSFs derived from the *HST* NICMOS images of the target galaxies, and noise was added to yield surface brightness profile errors similar to those of the target galaxies. Surface brightness profiles were derived for each simulated galaxy image by fitting ellipses, using the same fitting parameters that were employed for the derivation of the profiles for the program galaxies. The radial extent of the profiles was somewhat lower than that of the program galaxies, but this should not affect the results, given that, as we show below, disk parameters were accurately reproduced with their current radial extent. The profiles were fitted with combinations of Sérsic, exponential, and nuclear components, using the same code used for the program galaxies. As a test for any tendency of the fitting code to add nonexistent nuclear components, all models were fitted with and without nuclear components in the fitting function.

We found that nuclear Gaussian components are particularly difficult to reproduce. We suspect that the quadratic dependence of the Gaussian function on  $r$  made the fits unstable. Because of the failure with synthetic profiles, we do not present fits to the program galaxies employing Gaussian nuclear components. We note, however, that such fits yielded results that were generally consistent with the results of PS or exponential nuclear components: galaxies well modeled with inner PSs yielded good fits with very narrow Gaussians, and galaxies that required

an inner exponential component yielded good fits with broad Gaussians as well.

Results from the simulations are summarized in Table 5, which lists mean offsets (measured *minus* input) and rms deviations for each group of models. For the statistics, we group together pure Sérsic+exponential (se) models and PS+Sérsic+exponential (pse) models, which show similar uncertainties, and list models with inner exponentials (ese) separately; differences between the two sets are small anyway. Disk parameters are recovered with high accuracy. Uncertainties for bulge parameters are only somewhat larger and are asymmetric: we tend to recover fainter  $\mu_e$  ( $0.2-0.3$  mag arcsec $^{-2}$ ) and larger  $R_e$  ( $\Delta[\log(R_e)] \sim 0.05$ ). Such average uncertainties are probably overestimates, as the simulated models include inner components more luminous and more extended than seen in our program galaxies.

Point sources are recovered with an offset of  $\sim 0.3$  mag. Most likely, this offset arises from the fractional light in the secondary maximum of the NICMOS PSF (0.5 mag outside 2 pixels for F160W; Holfeltz & Calzetti 1999). The width of our Moffat PSF (FWHM =  $0.131''$ ) was set to match the main peak of the NICMOS PSF; hence, the light in the wings gets unaccounted for. A Moffat width of  $\sim 0.19''$  would greatly reduce such an offset, but at the price of losing spatial resolution; therefore, we adopt the narrower PSF and simply apply a 0.31 mag aperture correction to the PS magnitudes.

For inner exponentials, models with  $\mu_{0,2} > 1$  mag fainter than the Sérsic's  $\mu_0$  (Sérsic) get lost in the noise while, at the bright end, models with  $\mu_{0,2} - \mu_0(\text{Sérsic}) < -2$  yield inner profiles dominated by the inner exponential, which are quite unlike those of real galaxies. The statistics shown in Table 5 correspond to the range between those limits, which we split in bright and faint ranges as shown in the notes to the table. The PSF wings affect inner exponential components by making their derived

TABLE 3  
PHYSICAL PARAMETERS FOR THE DISK AND BULGE COMPONENTS

NGC (1)	$M_{K,\text{bulge}}$ (2)	$M_{K,\text{disk}}$ (3)	$B/D$ (4)	$\mu_0$ (5)	$\log h$ (6)	$\mu_e$ (7)	$\log R_e$ (8)	$\log n$ (9)
5326.....	$-22.96 \pm 0.17$	$-22.98 \pm 0.14$	0.98	$17.94 \pm 0.04$	$0.455 \pm 0.004$	$15.69 \pm 0.35$	$-0.23 \pm 0.07$	$0.41 \pm 0.07$
5389.....	$-22.17 \pm 0.14$	$-23.19 \pm 0.09$	0.39	$17.66 \pm 0.04$	$0.392 \pm 0.004$	$14.66 \pm 0.35$	$-0.58 \pm 0.07$	$0.13 \pm 0.07$
5422.....	$-21.86 \pm 0.10$	$-22.77 \pm 0.13$	0.43	$17.84 \pm 0.12$	$0.374 \pm 0.014$	$15.26 \pm 0.22$	$-0.53 \pm 0.05$	$0.31 \pm 0.04$
5443.....	$-20.76 \pm 0.26$	$-23.00 \pm 0.24$	0.13	$18.03 \pm 0.04$	$0.460 \pm 0.004$	$15.06 \pm 0.35$	$-0.77 \pm 0.07$	$0.23 \pm 0.07$
5475.....	$-20.98 \pm 0.14$	$-22.41 \pm 0.08$	0.27	$17.47 \pm 0.04$	$0.206 \pm 0.004$	$16.10 \pm 0.35$	$-0.57 \pm 0.07$	$0.33 \pm 0.07$
5577.....	$-18.20 \pm 0.13$	$-21.93 \pm 0.15$	0.03	$18.85 \pm 0.12$	$0.378 \pm 0.014$	$18.36 \pm 0.22$	$-0.61 \pm 0.05$	$0.04 \pm 0.04$
5587.....	$-20.26 \pm 0.16$	$-22.78 \pm 0.11$	0.10	$17.56 \pm 0.04$	$0.321 \pm 0.004$	$15.46 \pm 0.35$	$-0.71 \pm 0.07$	$-0.15 \pm 0.07$
5689.....	$-22.27 \pm 0.31$	$-23.68 \pm 0.29$	0.27	$16.80 \pm 0.04$	$0.337 \pm 0.004$	$14.31 \pm 0.35$	$-0.57 \pm 0.07$	$-0.07 \pm 0.07$
5707.....	$-21.90 \pm 0.15$	$-22.78 \pm 0.10$	0.44	$17.73 \pm 0.04$	$0.350 \pm 0.004$	$15.30 \pm 0.35$	$-0.43 \pm 0.07$	$-0.11 \pm 0.07$
5719.....	$-22.88 \pm 0.16$	$-22.45 \pm 0.12$	1.49	$18.51 \pm 0.04$	$0.467 \pm 0.004$	$15.48 \pm 0.35$	$-0.26 \pm 0.07$	$0.29 \pm 0.07$
5746.....	$-22.31 \pm 0.10$	$-24.85 \pm 0.13$	0.10	$17.13 \pm 0.12$	$0.596 \pm 0.014$	$15.06 \pm 0.22$	$-0.51 \pm 0.05$	$0.19 \pm 0.04$
5838.....	$-22.59 \pm 0.16$	$-23.10 \pm 0.12$	0.62	$17.59 \pm 0.04$	$0.401 \pm 0.004$	$14.91 \pm 0.35$	$-0.41 \pm 0.07$	$0.16 \pm 0.07$
5854.....	$-21.75 \pm 0.22$	$-22.92 \pm 0.19$	0.34	$17.42 \pm 0.04$	$0.282 \pm 0.004$	$16.20 \pm 0.35$	$-0.40 \pm 0.07$	$0.27 \pm 0.07$
5879.....	$-19.35 \pm 0.25$	$-21.81 \pm 0.26$	0.10	$16.38 \pm 0.12$	$-0.174 \pm 0.014$	$16.47 \pm 0.22$	$-0.87 \pm 0.05$	$0.35 \pm 0.04$
5965.....	$-22.81 \pm 0.21$	$-24.63 \pm 0.23$	0.19	$18.10 \pm 0.12$	$0.789 \pm 0.014$	$15.98 \pm 0.22$	$-0.24 \pm 0.05$	$0.44 \pm 0.04$
6010.....	$-21.79 \pm 0.35$	$-23.00 \pm 0.36$	0.33	$17.35 \pm 0.12$	$0.328 \pm 0.014$	$14.90 \pm 0.22$	$-0.62 \pm 0.05$	$0.33 \pm 0.04$
6504.....	$-23.68 \pm 0.10$	$-24.34 \pm 0.13$	0.55	$17.91 \pm 0.12$	$0.704 \pm 0.014$	$16.20 \pm 0.22$	$-0.00 \pm 0.05$	$0.42 \pm 0.04$
7457.....	$-19.87 \pm 0.23$	$-21.84 \pm 0.20$	0.16	$17.29 \pm 0.04$	$0.125 \pm 0.004$	$16.22 \pm 0.35$	$-0.69 \pm 0.07$	$0.30 \pm 0.07$
7537.....	$-19.47 \pm 0.22$	$-23.07 \pm 0.23$	0.04	$16.76 \pm 0.12$	$0.114 \pm 0.014$	$17.03 \pm 0.22$	$-0.75 \pm 0.05$	$0.24 \pm 0.04$

NOTES.—This table lists parameters for the disk and bulge, corrected from measurement offsets as described in § 4. Absolute magnitudes are given in the  $K$  band. Surface brightnesses are given in  $H$ -band  $\text{mag arcsec}^{-2}$ . Both magnitudes and surface brightnesses are corrected for Galactic extinction, cosmological dimming, and  $K$ -correction. Scale lengths are in kiloparsecs; for bulges, they refer to the geometric mean axis  $(ab)^{1/2}$  of the measured ellipse, while for disks, scale lengths are scaled to the major axis, assuming an inclination given by the disk ellipticity. Col. (1): Galaxy NGC number. Col. (2–3) Bulge and disk  $K$ -band absolute magnitudes, from the galaxy  $K$ -band absolute magnitude and the bulge-disk ratio from col. (4). Col. (4): Luminosity ratio between the bulge and main disk, from best-fit parameters ( $H$  band). Col. (5) Disk face-on extrapolated central surface brightness. Col. (6): Disk scale length. Col. (7): Bulge effective surface brightness. Col. (8) Bulge effective radius. Col. (9): Bulge Sérsic index.

scale lengths about 10%–20% higher, while making the central surface brightness fainter. Total magnitudes show an uncertainty of a few tenths of magnitude—larger for the fainter components, as expected.

Three main lessons derive from the simulations.

1. Bulge and outer disk parameters are robust to the presence of nuclear components and to the choice of PSF; in particular, our fitting code does not artificially introduce nuclear components to pure Sérsic+exponential profiles with a high- $n$  Sérsic component.

2. A moderate level of parameter coupling is present for the bulge: derived  $\mu_e$  are probably faint by  $\sim 0.2$ – $0.3 \text{ mag arcsec}^{-2}$ , while  $\log(R_e)$  are probably overestimated by  $\sim 5\%$ .

3. Nuclear unresolved sources are accurately recovered once an aperture correction of  $\sim 0.3 \text{ mag}$  is applied.

## 5. RESULTS

Physical parameters for bulges, disks, and nuclear components are listed in Tables 3 and 4. Corrections for measurement offsets, derived from the simulations (§ 4), have been added where applicable (Table 5); rms error estimates can also be found in Table 5.

The first result of our analysis is that nuclear sources are quite common in disk galaxy bulges. Excesses over the Sérsic fit to the bulge are measured in 17 out of 19 galaxies. Over half (11) of those are extended; six can be modeled with an exponential profile, while five harbor a central unresolved source in addition to the exponential. The remaining six galaxies with central excesses can be modeled with an unresolved source. These results are not new. Nuclear sources, resolved or unresolved at the scale of the *HST* instruments, have been reported by others for bulges (Carollo et al. 1998; Paper I), ellipticals and early-type bulges (R01; Ravindranath et al. 2001; F06), dwarf ellipticals (Stiavelli et al. 2001; Graham & Guzmán 2003; Côté et al. 2006), and late-type

spirals (Böker et al. 2002). The variety of detection methods and functions used by these teams to model the underlying light distributions suggests that nuclear components are not an artifact of the model fitting but are real components of many galaxy nuclei.

Absolute magnitudes of the nuclei are plotted in Figure 2 against the  $K$ -band absolute magnitude of the bulge, bulge central velocity dispersion, bulge color, and disk ellipticity. Nuclei are, on the mean,  $4.4 \pm 1.9 \text{ mag}$  fainter than their host bulges, and  $6.1 \pm 1.7 \text{ mag}$  fainter than their host galaxies, although some of the extended components are only 2 mag fainter than their host bulge (e.g., NGC 5587; see Table 4). In general, nuclei are minor contributors to the galaxy light.

If structural components are linked to formation events in the history of the host galaxies, we may inquire whether nuclei are recent additions to the galaxy, or old, perhaps the seed of the formation of the bulge or of the entire galaxy. If galaxy centers host a supermassive black hole, whose formation and growth went through a phase of positive feedback with the formation of the galaxy (Silk 2005), are the nuclei detected here connected in any way to such positive feedback (McLaughlin et al. 2006)? In the following subsections we further analyze the extended and unresolved nuclear components.

### 5.1. Nuclear Extended Components

The nuclear extended components have absolute  $K$ -band magnitudes in the range  $-16 > M_{K,\text{ext}} > -20$ . Their scale lengths are  $\sim 5$ – $60 \text{ pc}$ , or about 100 times smaller than the outer disk scale lengths and 20 times smaller than the effective radii of the bulge (for NGC 5719, an extreme case,  $R_e$  is 100 times higher than  $h_2$ ). But they have very high densities. Extrapolated central surface brightnesses are in the range  $11 < \mu_H < 15$ , typically 5 mag brighter than the  $\mu_0$  of the main galaxy disk. In many cases,

TABLE 4  
PHYSICAL PARAMETERS FOR THE NUCLEAR COMPONENTS

NGC (1)	$M_{K,PS}$ (2)	$M_{K,E2}$ (3)	$\mu_{0,2}$ (4)	$\log(h_2)$ (5)	Fit Type (6)
5326.....	...	$-19.21 \pm 0.47$	$11.58 \pm 0.94$	$-1.60 \pm 0.18$	ese
5389.....	...	$-17.07 \pm 0.47$	$11.71 \pm 0.94$	$-2.00 \pm 0.18$	ese
5422.....	$-14.79 \pm 0.35$	...	...	...	pse
5443.....	...	$-15.99 \pm 0.47$	$11.12 \pm 0.94$	$-2.34 \pm 0.18$	ese
5475.....	$-15.00 \pm 0.35$	$-18.70 \pm 0.26$	$13.11 \pm 0.45$	$-1.40 \pm 0.04$	pese
5577.....	...	...	...	...	se
5587.....	...	$-18.23 \pm 0.26$	$14.42 \pm 0.45$	$-1.23 \pm 0.04$	ese
5689.....	...	$-19.28 \pm 0.26$	$13.50 \pm 0.45$	$-1.20 \pm 0.04$	ese
5707.....	$-16.16 \pm 0.35$	$-19.77 \pm 0.26$	$13.13 \pm 0.45$	$-1.18 \pm 0.04$	pese
5719.....	...	$-16.64 \pm 0.47$	$10.45 \pm 0.94$	$-2.34 \pm 0.18$	ese
5746.....	$-14.72 \pm 0.35$	...	...	...	pse
5838.....	$-16.13 \pm 0.35$	$-20.16 \pm 0.26$	$11.81 \pm 0.45$	$-1.36 \pm 0.04$	pese
5854.....	$-16.96 \pm 0.35$	$-19.14 \pm 0.26$	$11.84 \pm 0.45$	$-1.56 \pm 0.04$	pese
5879.....	$-13.28 \pm 0.35$	...	...	...	pse
5965.....	...	...	...	...	se
6010.....	$-15.78 \pm 0.35$	...	...	...	pse
6504.....	$-16.71 \pm 0.35$	...	...	...	pse
7457.....	$-15.71 \pm 0.35$	$-16.29 \pm 0.47$	$12.40 \pm 0.94$	$-2.02 \pm 0.18$	pese
7537.....	$-15.34 \pm 0.35$	...	...	...	pse

NOTES.—This table lists parameters for nuclear components, corrected from measurement offsets as described in § 4. Nuclear source absolute magnitudes are given in the  $K$  band, using  $H - K = 0.23$ . Surface brightness  $\mu_{0,2}$  is given in  $H$ -band mag arcsec $^{-2}$ . Both magnitudes and surface brightnesses are corrected for Galactic extinction, cosmological dimming, and  $K$ -correction. Scale lengths are in kiloparsecs and have been scaled to the major axis, assuming an inclination given by the disk ellipticity. Col. (1): Galaxy NGC number. Col. (2):  $K$ -band absolute magnitude of the central unresolved source. Col. (3):  $K$ -band absolute magnitude of the nuclear exponential component. Col. (4): Face-on extrapolated central surface brightness of the nuclear exponential component. Col. (5) Scale length of the nuclear exponential component. Col. (6): Fit type code—se: Sérsic bulge and exponential outer disk; pse: se plus a nuclear point source; ese: se plus an inner exponential component; pese: se plus a nuclear point source and a nuclear exponential component.

nuclear extended components dominate the surface brightness profile inward of  $1''$  (see Fig. 1).

On the basis of their luminosity distribution (Fig. 2a), the nuclear extended components might be a heterogeneous family. Seven galaxies draw a bright sequence with absolute magnitudes  $-18 > M_{K,ext} > -20$ , or 3%–15% of the bulge luminosity, while the four remaining cases show fainter luminosities ( $-16 > M_{K,ext} > -17$ , or 0.3%–3% of the bulge luminosity) that overlap with the luminosities of the unresolved sources. These fainter objects are also the smallest ( $h_2 < 10$  pc) and densest, and may be instances of nuclear clusters that we managed to resolve in our images. The objects in the brighter sequence are also more extended ( $25 \text{ pc} < h_2 < 60 \text{ pc}$ ); five of the seven cases themselves harbor nuclear unresolved sources, and their sizes and fractional luminosities resemble those of inner disks in elliptical galaxies (Scorza & Bender 1995; Scorza & van den Bosch 1998). These properties give clues that such objects might have a different nature and formation mechanism than their more compact counterparts. The presence of more extended components than nuclear clusters indicates that structural deviations from the Sérsic profile in the nuclei of early-type disk galaxies are not restricted to nuclear star clusters: more extended structures, which we show below to be flattened systems, also cause the bulge profile to deviate from the Sérsic functional form.

Scale lengths and central surface brightnesses for inner and outer disks are plotted together in Figure 3. They correlate quite well, both for the nuclear disks alone,

$$\frac{I_{0,2}}{L_{K,\odot}} = 10^{-3.12 \pm 0.16} \left( \frac{h_2}{10 \text{ pc}} \right)^{-1.26 \pm 0.31} \quad (3)$$

( $S_R = 0.83$ ;  $P_{\text{null}} = 8.9 \times 10^{-3}$ ), and for inner and outer disks together,

$$\frac{I_0}{L_{K,\odot}} = 10^{-5.30 \pm 0.12} \left( \frac{h}{\text{kpc}} \right)^{-1.07 \pm 0.05} \quad (4)$$

( $S_R = 0.91$ ;  $P_{\text{null}} = 8.4 \times 10^{-7}$ ). In the above equations,  $I_0$  denotes central intensity in the  $K$  band, in units of  $K$ -band solar luminosities per square arcsecond. Both relations are consistent with each other, suggesting that  $I_0 \sim h^{-1}$ , or  $L \sim h$ . Caution is needed when interpreting these relations, given the important selection effects operating on the detection of inner components. We saw in § 4 that detection of inner disks is broadly constrained at  $-2 < \mu_{0,2} - \mu_{0,\text{Sérsic}} < 1$ . In practice, we have found  $\langle \mu_{0,2} - \mu_{0,\text{Sérsic}} \rangle = -0.05 \pm 0.81$ , i.e., only those inner disks that match the central surface brightness of the bulge's Sérsic profile are detected, and any inner disks much fainter than that limit would go undetected by our fitting code. Hence, equations (3) and (4) describe the upper envelope of inner disk surface densities. Similarly, the distribution of our large-scale disks in this diagram is known to define an upper envelope of points (Graham & de Blok 2001).

We seek clues on the nature of nuclear extended components by relating their structural parameters to isophotal, dynamical, and color information. Figures with such information are shown for each galaxy in the Appendix.

All of the 11 galaxies with inner extended components show corresponding disk isophotes in the inner arcsecond (see Fig. 8). The association of extended components with disk isophotes is nearly one to one, as only three galaxies with disk isophotes in their bulges (NGC 5746, 5965, and 7537) do not require an

TABLE 5  
PARAMETER UNCERTAINTIES

PARAMETER (1)	se, pse MODELS		ese MODELS	
	$\Delta$ (2)	$\sigma$ (3)	$\Delta$ (4)	$\sigma$ (5)
Outer Exponential (Disk)				
$\mu_0$ .....	0.089	0.123	-0.010	0.036
$\log h$ .....	0.007	0.014	-0.003	0.004
Magnitude.....	0.029	0.085	0.010	0.046
$-2.5 \log (D/T)$ .....	0.066	0.101	0.012	0.046
Sérsic (Bulge)				
$\mu_e$ .....	0.060	0.224	0.205	0.348
$\log R_e$ .....	0.029	0.052	0.044	0.070
$\log n$ .....	-0.007	0.035	0.007	0.072
Magnitude.....	-0.090	0.106	-0.019	0.150
$-2.5 \log (B/D)$ .....	-0.118	0.159	-0.025	0.163
$-2.5 \log (B/T)$ .....	-0.052	0.071	-0.017	0.118
Nuclear Unresolved Source				
Magnitude (PS).....	0.310	0.351	...	...
Nuclear Exponential (Bright Range)				
$\mu_{0,2}$ .....	...	...	0.45	0.45
$\log (h_2)$ .....	...	...	0.09	0.04
Magnitude (2).....	...	...	-0.003	0.26
Nuclear Exponential (Faint Range)				
$\mu_{0,2}$ .....	...	...	0.81	0.94
$\log (h_2)$ .....	...	...	0.18	0.18
Magnitude (2).....	...	...	-0.09	0.47

NOTE.—For each parameter, Col. (2) gives the mean difference (measured minus input) and rms deviation for se, pse synthetic models. Col (3) gives the same quantities for ese models. For the nuclear exponentials, bright range (faint range) denotes models in which the inner exponential is brighter (fainter) than the Sérsic component at  $R = 0.1''$ . See § 4.

inner exponential component to fit the surface brightness profile. NGC 5746, with a peanut-shaped bulge, shows disklike isophotes in the bulge–outer disk transition region; NGC 5965, another prototype peanut-shaped bulge, has a very strong positive  $c_4$  disk coefficient in the entire bulge region, suggesting that the entire

bulge is disklike (see, e.g., Bureau et al. 2006); and finally, NGC 7537 (Sbc) has a faint bulge and low velocity dispersion ( $\sigma = 42 \text{ km s}^{-1}$ ). Hence, the bulges in these three galaxies really look like disks, and fall under the definitions of pseudobulge (Kormendy & Kennicutt 2004). For the rest of the sample, inner disklike isophotes are associated with nuclear extended components.

Such correspondence suggests that inner extended components of the surface brightness profiles trace true structural components of the galaxy nuclei, with flattened shapes. On the basis of SAURON three-dimensional spectroscopy, similar flat kinematically decoupled components aligned with the main galaxy disk have recently been reported for early-type spirals by Falcón-Barroso et al. (2006; see also McDermid et al. 2006). The simple conjecture that they are inner disks, bars, or nuclear rings is supported by the kinematic data, which show velocities consistent with circular motions and often show velocity dispersion minima. Smaller, but also extended, “flattened clusters” have been found in imaging programs for later-type spirals by Seth et al. (2006). For our galaxies, the typical outer radius of the positive  $c_4$  structures is a few hundred parsecs, which is a typical size of inner bars in double-bar galaxies (Erwin & Sparke 2002; Erwin 2004).

For our galaxies, nuclear features in the velocity dispersion profiles (see Fig. 8) are not associated with the presence of nuclear extended components. In the inner arcsecond, typically where nuclear components have a strong contribution to the total surface brightness, most velocity dispersion profiles are quite flat, with specific instances of central peaks or drops. These profiles, from minor-axis spectra taken with the William Herschel Telescope (WHT) Intermediate Dispersion Spectrograph and Imaging System (ISIS), have a  $0.3''$  sampling and a seeing of around  $1.0''$  (Falcón-Barroso et al. 2003). Clearly, two-dimensional spectroscopy at subarcsecond resolution is required for a kinematic characterization of the nuclear extended components.

The colors of the extended nuclear components are quite red, and, as shown in Paper I, they correspond to a stellar population reddened with a mean of  $A_V = 0.5\text{--}1.0$ . The color profiles, however, are generally very smooth (see Fig. 8). This suggests that the stellar populations of the nuclear extended components are not very distinct from those of the surrounding bulges. In particular, despite signs of nuclear star formation (Paper I), the bulk of their stellar populations are not recent additions to the galaxy. Note that the combination of blue and NIR colors is particularly sensitive to population age. In later type spirals, the nuclear flattened clusters are bluer than the host spheroid (Seth et al. 2006),

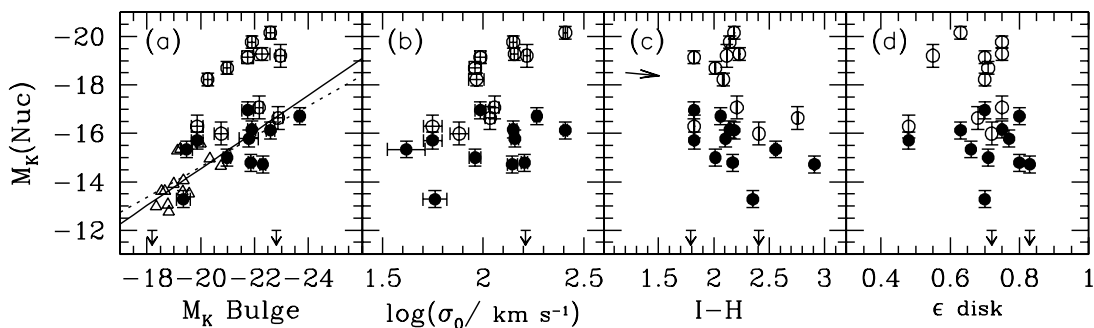


FIG. 2.—Absolute  $K$ -band magnitude of the nuclear components against: (a)  $K$ -band absolute magnitude of the bulge. *Filled circles*: Unresolved components in bulges. *Open circles*: Resolved components in bulges. *Triangles*: Nuclear components in dwarf ellipticals from Graham & Guzmán (2003). The dotted line is an orthogonal regression to the bulge unresolved components (see eq. [5]), while the solid line is an orthogonal regression to the bulge and dE unresolved components together (eq. [6]). (b) Aperture-corrected central velocity dispersion, from Table 1. (c) Central  $I - H$  color, from *HST* NICMOS F160W and WFPC2 F814W images (Paper I). An extinction vector for normal Galactic extinction of  $A_V = 1 \text{ mag}$  (Rieke & Lebofsky 1985) is plotted in the top left. (d) Ellipticity of the outer disk, from two-dimensional bulge-disk decomposition in  $K$ -band images (APB95). Upper limits are given for the galaxies without detected nuclear components; one of those (NGC 5577) does not have a central velocity dispersion measurement. [See the electronic edition of the *Journal* for a color version of this figure.]

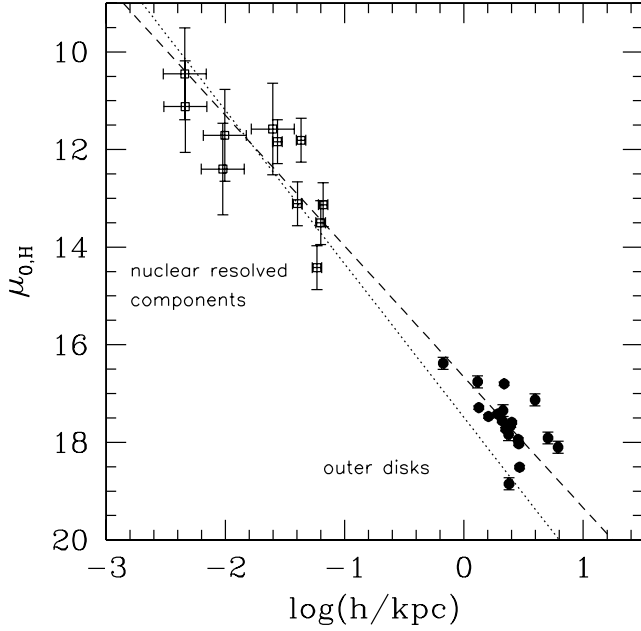


FIG. 3.—Disk scale length in kiloparsecs vs. extrapolated central surface brightness, for inner extended components, and for main galaxy disks. *Dotted line*: Orthogonal regression to the nuclear-resolved components (eq. [3]). *Dashed line*: Orthogonal regression to both nuclear resolved components and outer disks (eq. [4]). [See the electronic edition of the *Journal* for a color version of this figure.]

perhaps indicating an extended star formation history for the nuclear structures that continues today for late-type spirals (see also Walcher et al. 2006), but has finished in most earlier-type disk galaxies.

### 5.2. Nuclear Unresolved Sources

As previously noted, we detect unresolved sources (referred to as PSs) in 11 of our 19 galaxies; 5 of these coexist with an inner exponential. Our detection frequency is similar to that reported in previous studies: Ravindranath et al. (2001) reported a 50% detection fraction, Böker et al. (2002) found nuclear PSs in 76% of their sample, and Côté et al. (2006) reported a fraction of 66%–88% of nucleated early-type galaxies from the Advanced Camera for Surveys (ACS) Virgo Cluster Survey.

For our sample, the absence of active galactic nuclei (AGNs), and the nuclear colors, suggest that light from the PSs is stellar in origin, i.e., that they are nuclear star clusters. A similar conclusion was reached by Phillips et al. (1996) and Carollo et al. (1998), whereas Ravindranath et al. (2001) argued for a nonstellar origin for the PS light on the basis of the high frequency of AGNs in their sample. In what follows we assume the PSs to be nuclear clusters, although we recognize that, in general, AGN contribution to nuclear emission may be important in specific samples.

Absolute magnitudes are in the range  $-13 > M_{K,PS} > -17$  (Table 4), on the mean 6 mag fainter than their host bulges ( $K$ -band luminosity ratio of 0.4%). Their luminosities correspond to 10–20 globular clusters, quite comparable to nuclei in nucleated Virgo ellipticals (Côté et al. 2006). These absolute magnitudes do not vary systematically with galaxy inclination (Fig. 2*d*), suggesting that extinction in the parent disks does not affect  $M_{K,PS}$ . Extinction at the nuclei themselves does have a small effect on  $M_{K,PS}$ . We show for reference an  $A_V = 1$  mag extinction vector in Figure 2*c*.

We showed in Paper II that  $M_{K,PS}$  correlates with the bulge absolute magnitude, a result later confirmed by Rossa et al. (2006)

using optical imaging. The correlation given in equation (1) of Paper II was derived from fits to 17 objects, using a slightly wider PSF (0.19" FWHM) than is used here (0.131"). For the fits presented here, an orthogonal regression to the  $M_{K,PS}$ - $M_{K,bul}$  distribution gives

$$\frac{L_{K,PS}}{L_{K,\odot}} = 10^{7.70 \pm 0.17} \left( \frac{L_{K,bul}}{10^{10} L_{K,\odot}} \right)^{0.63 \pm 0.37} \quad (5)$$

(using  $M_{K,\odot} = 3.41$ ; Allen 1973), consistent with what we gave in Paper II. However, with only 11 data points and a significant scatter, the relation is not statistically significant for this sample ( $S_R = 0.43$ ;  $P_{null} = 0.18$ ). Graham & Guzmán (2003), who analyzed Coma dwarf elliptical (dE) *HST* WFPC2 F606W galaxy surface brightness profiles using the same fitting code as the present paper, also find a scaling between PS and bulge luminosity, with a consistent slope of  $0.87 \pm 0.26$ . Their data points are given in Figure 2*a*.<sup>5</sup> Inasmuch as the nuclei of our bulges and those of the Coma dEs are similar structures, we may use the combined sample to derive the scaling of nuclear unresolved sources with spheroid luminosity. We find

$$\frac{L_{K,PS}}{L_{K,\odot}} = 10^{7.75 \pm 0.15} \left( \frac{L_{K,bul}}{10^{10} L_{K,\odot}} \right)^{0.76 \pm 0.13} \quad (6)$$

( $S_R = 0.72$ ;  $P_{null} = 4.0 \times 10^{-4}$ ). We transform equation (6) into a mass relation; i.e.,

$$\frac{\mathcal{M}_{PS}}{\mathcal{M}_{\odot}} = 10^{7.73 \pm 0.16} \left( \frac{\mathcal{M}_{bul}}{10^{10} \mathcal{M}_{\odot}} \right)^{0.76 \pm 0.13}, \quad (7)$$

where  $M/L_K = 0.8$  has been assumed for nuclei and bulges, from Bell & de Jong (2001), for the typical colors of bulge populations. The normalization is insensitive to the choice of  $M/L_K$  because its slope is close to unity; using the more extreme  $M/L_K = 0.5$  would yield a nearly identical normalization term of  $10^{7.68 \pm 0.16}$ .

Equation (7) may be compared to scaling regressions found in other studies of nuclear clusters. F06 found  $\mathcal{M}_{nuc} \sim \mathcal{M}_{bul}^{1.32 \pm 0.25}$ , which is  $\sim 2 \sigma$  from our slope. And, for their so-called CMOs, a class encompassing central supermassive black holes (SMBHs) and central star clusters, F06 found, when fixing the exponent to unity,

$$\frac{\mathcal{M}_{CMO}}{\mathcal{M}_{\odot}} = 10^{7.26 \pm 0.47} \left( \frac{\mathcal{M}_{gal}}{10^{10} \mathcal{M}_{\odot}} \right)^{1.0}. \quad (8)$$

while for a sample of galaxies with kinematic SMBH mass determinations, Häring & Rix (2004, hereafter HR04) infer

$$\frac{\mathcal{M}_{\bullet}}{\mathcal{M}_{\odot}} = 10^{7.08 \pm 0.10} \left( \frac{\mathcal{M}_{bul}}{10^{10} \mathcal{M}_{\odot}} \right)^{1.12 \pm 0.06}. \quad (9)$$

Figure 4 shows the host spheroid mass against the nuclear mass of unresolved bulge and dE components. For comparison

<sup>5</sup> After applying a constant color term, F606W -  $K = 2.7$ . This scaling corresponds to an old population with 0.4 times solar metallicity, using the models of Vazdekis et al. (1996); a lower metallicity would make the total and nuclear luminosities of the dE fainter.

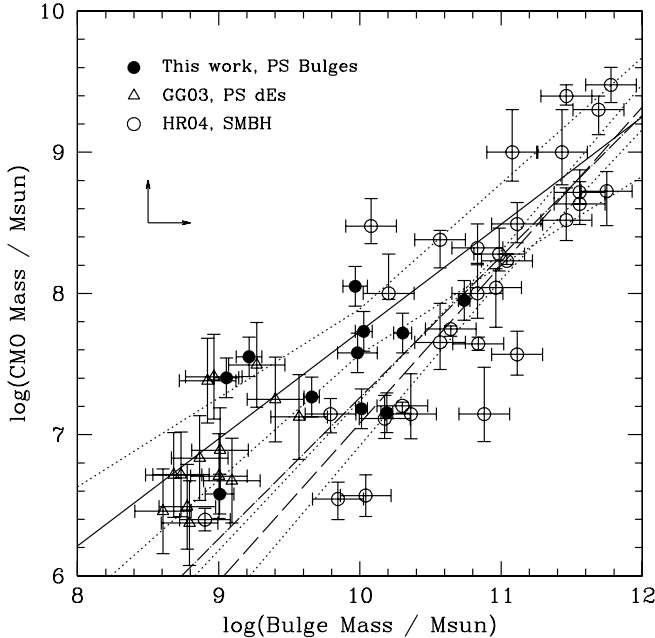


FIG. 4.—Spheroid mass plotted against the mass of the compact massive object. *Filled circles*: This work; bulge mass vs. nuclear unresolved source mass. *Triangles*: Coma dwarf ellipticals from Graham & Guzmán (2003). The above are photometric masses, in solar units, derived from the  $K$ -band luminosities assuming  $M/L_K = 0.8$ ; see § 5.2. *Open circles*: Ellipticals and bulges with central SMBHs, from HR04. *Solid line*: Regression for bulges and dEs (eq. [7]). *Long-dashed line*: Bisector linear regression for the sample of HR04; see eq. (9). *Dotted lines*:  $\pm 1 \sigma$  range of acceptable fits. *Dot-dashed line*: The relation between CMOs and galaxy mass derived by F06 under the assumption of a linear scaling (eq. [8]). [See the electronic edition of the Journal for a color version of this figure.]

we plot the HR04 distribution of  $\mathcal{M}_\bullet$  versus host mass. The regressions provided by HR04 (eq. [9]), F06 (eq. [8]), and us (eq. [7]) are plotted as well. The distribution of  $\mathcal{M}_{\text{PS}}$  converges with that of the  $\mathcal{M}_\bullet$  regression at the high-mass end, but it progressively deviates as we move to lower spheroid masses. Both our distribution of  $\mathcal{M}_{\text{PS}}$  and HR04’s distribution of  $\mathcal{M}_\bullet$  show a large scatter at  $\log(\mathcal{M}_{\text{bul}}) \leq 10$ ; hence, the slopes of the regressions have large uncertainties in that mass domain. However, the nuclear cluster masses are systematically above the extrapolation of the HR04 or F06 relations. From equation (7), nuclei fractional mass ( $\mathcal{M}_{\text{PS}}/\mathcal{M}_{\text{bul}}$ ) increases from 0.19%, identical to central black hole fractional masses, to 0.71%, as  $\mathcal{M}_{\text{bul}}$  decreases from  $10^{11.5} \mathcal{M}_\odot$  to  $10^{9.5} \mathcal{M}_\odot$ . We are aware that different mass determinations are being compared in Figure 4 (photometric masses for our data, virial masses for F06, and masses derived from Jeans equation modeling for HR04). Nevertheless, we argue that the observed offset between our unresolved components and the SMBH relations from either HR04 or F06 cannot be explained by uncertainties in our mass determinations. Bridging the offset by changing our assumed  $M/L_K$  would require  $M/L_K$  of nuclei to be lower than those of their parent galaxies by a factor of  $\sim 4$ , which is implausible for stellar populations without signs of vigorous star-forming activity. Using dynamical masses for our bulges instead of the photometric masses does not help either: applying for consistency the same form of the virial mass used by F06,

$$\mathcal{M}_{\text{bul,dyn}} \equiv 5R_e \frac{\sigma^2}{G}, \quad (10)$$

the offset actually increases ( $\mathcal{M}_{\text{bul,dyn}}$  are on the mean a factor 2 below the stellar mass  $\mathcal{M}_{\text{bul}}$ ), which shifts our points to the left,

away from the F06 relation; such discrepancy indicates that equation (10) underestimates the true dynamical mass of the bulges—most likely due to ignoring the rotational kinetic energy.

We thus cannot reproduce F06’s result that nuclear star cluster masses fall onto the same linear relation as defined by more massive central black holes. Any CMO–bulge mass relation that encompasses both central black holes and nuclear star clusters must be nonlinear for bulge masses of, say,  $\mathcal{M}_{\text{bul}} \leq 10^{10} \mathcal{M}_\odot$ . An orthogonal regression to the nuclear star cluster masses and the black hole masses, against the host bulge mass, gives

$$\frac{\mathcal{M}_{\text{CMO}}}{\mathcal{M}_\odot} = 10^{7.51 \pm 0.06} \left( \frac{\mathcal{M}_{\text{bul}}}{10^{10} \mathcal{M}_\odot} \right)^{0.84 \pm 0.06} \quad (11)$$

We conjecture that F06 found a linear  $\mathcal{M}_{\text{CMO}}-\mathcal{M}_{\text{bul}}$  relation because, near the low-mass end, their sample includes many S0s. When deriving virial masses using equation (10), because their  $R_e$  values derive from single Sérsic fits to the galaxy profiles (Côté et al. 2006), spheroid masses are probably overestimated for all of their S0 galaxies, which is roughly half of their sample. We show in Paper IV that the mean ( $\pm$  standard deviation) bulge-to-total ratio for the eight S0 and S0a galaxies in our sample is  $\langle B/T \rangle = 0.25 \pm 0.09$ , slightly below the mean value of  $0.28 \pm 0.16$  derived from the fits in APB95. Using a sample from the Near-Infrared S0 Survey (NIRS0S) survey, Laurikainen et al. (2005) reported a similar result,  $\langle B/T \rangle = 0.24 \pm 0.11$ . So one may expect a downward correction to (half of) the F06 spheroidal masses of  $\sim 0.6$  dex, which would explain the different trends between F06 and us.

### 5.3. Nuclear Black Hole Masses

To further investigate the connection between star clusters and central SMBHs proposed by F06 and Wehner & Harris (2006), in this subsection we explore the scalings of SMBH mass  $\mathcal{M}_\bullet$ , nuclear cluster mass, and bulge mass. We estimate  $\mathcal{M}_\bullet$  using the expression

$$\log \mathcal{M}_\bullet = 4.02(\pm 0.32) \log \left( \frac{\sigma}{200} \right) + 8.13(\pm 0.06) \quad (12)$$

from Tremaine et al. (2002, hereafter T02), where  $\mathcal{M}_\bullet$  is in solar masses, and  $\sigma$  is the central velocity dispersion in kilometers per second. We show bulge masses against SMBH masses in Figure 5a. An orthogonal regression of our estimated  $\mathcal{M}_\bullet$  against  $\mathcal{M}_{\text{bul}}$  gives

$$\frac{\mathcal{M}_\bullet}{\mathcal{M}_\odot} = 10^{7.25 \pm 0.11} \left( \frac{\mathcal{M}_{\text{bul}}}{10^{10} \mathcal{M}_\odot} \right)^{1.72 \pm 0.26} \quad (13)$$

( $S_R = 0.84$ ;  $P_{\text{null}} = 5.6 \times 10^{-4}$ ). Such a strong relation is expected because it is largely a manifestation of the strong Faber-Jackson relation followed by our bulges. Our bulges follow  $L_{K,\text{bul}} \propto \sigma^{2.86 \pm 0.5}$  (see § 3.1.5 of Paper IV), and using  $\mathcal{M}_\bullet \propto \sigma^{4.02 \pm 0.32}$  we expect  $\mathcal{M}_\bullet \propto (\mathcal{M}_{\text{bul}})^{4.02/2.86} = (\mathcal{M}_{\text{bul}})^{1.41 \pm 0.31}$ , consistent with equation (13). Equation (13) is also consistent with that found by Laor (2001) for a sample of active and inactive galaxies, i.e.,  $\mathcal{M}_\bullet \propto (\mathcal{M}_{\text{bul}})^{1.53 \pm 0.14}$ . Our scaling lies  $2 \sigma$  from the relation found by HR04 (drawn in Fig. 5a) and formally departs  $2.8 \sigma$  from linearity (shown with a dashed line in Fig. 5a). We do not want to give much weight to this departure from linearity,

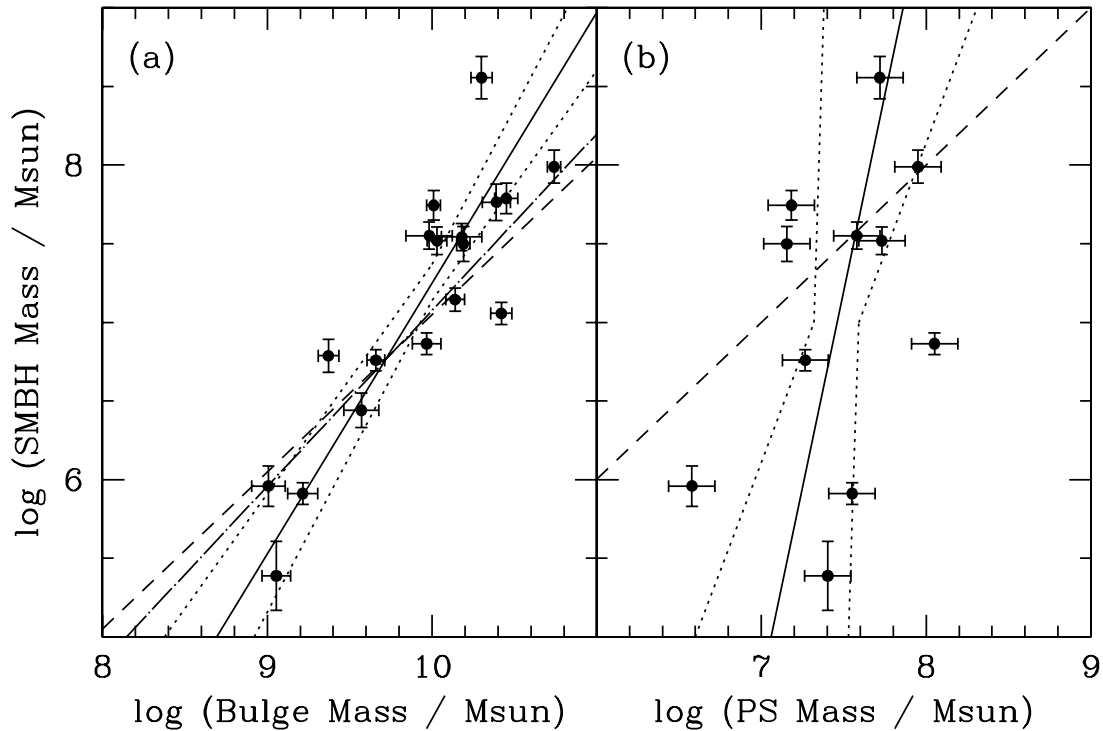


FIG. 5.—Central SMBH mass, estimated from the velocity dispersion following T02, plotted vs. (a) the photometric bulge mass and (b) the photometric mass of the nuclear unresolved sources. Photometric masses are derived from the  $K$ -band luminosities assuming  $M/L_K = 0.8$ ; see § 5.2. The solid lines in (a) and (b) correspond to eqs. (13) and (14), respectively, while dotted lines delineate the approximate region of acceptable fits given the  $1\sigma$  error bars in the fit coefficients. In (a), the dot-dashed line traces the SMBH mass–spheroid mass relation of HR04, while the dashed line traces a slope unity relation for reference. In (b), the dashed line is the locus where PS masses and SMBH masses are equal. [See the electronic edition of the *Journal* for a color version of this figure.]

given the small sample size and the fact that we are extrapolating the  $\mathcal{M}_\bullet$ - $\sigma$  relation faintward.

If central black holes and central star clusters are intimately related, the latter perhaps being failed black holes, then the  $\mathcal{M}_\bullet$ - $\sigma$  relation (eq. [12]) should be able to predict the nuclear cluster masses. We plot  $\mathcal{M}_{\text{PS}}$  (measured) against  $\mathcal{M}_\bullet$  (estimated) in Figure 5b, together with the result of an orthogonal regression to the nuclear star cluster–black hole mass distribution, which gives

$$\frac{\mathcal{M}_{\text{PS}}}{\mathcal{M}_\odot} = 10^{7.46 \pm 0.14} \left( \frac{\mathcal{M}_\bullet}{10^7 \mathcal{M}_\odot} \right)^{0.20 \pm 0.16} \quad (14)$$

( $S_R = 0.37$ ;  $P_{\text{null}} = 0.24$ ). The correlation is not statistically significant, partly due to the small sample size and the scatter of the data points. We report this regression to clarify that the slope of the relation is several sigma away from the value of 1 expected if the  $\mathcal{M}_\bullet$ - $\sigma$  relation had predicted the masses of all the star clusters. This occurs also when SMBH masses are computed following Merritt & Ferrarese (2001).

Wehner & Harris (2006) advocated a CMO transitional mass at  $10^7 \mathcal{M}_\odot$ . While our  $\mathcal{M}_\bullet$  scatter above and below this mass limit, all but one of our nuclear star clusters lie above it. Some bulges are already known to contain both a SMBH and a nuclear star cluster: NGC 7457, which is in our sample, and NGC 3384 (Wehner & Harris 2006). Curiously, above the  $10^7 \mathcal{M}_\odot$  limit, our nuclear star cluster masses agree with the predicted SMBH masses. Below the  $10^7 \mathcal{M}_\odot$  limit, cluster masses lie  $\sim 1$  dex above the extrapolation of the black hole mass relation (shown as a dashed line in Fig. 5b). Hence, again the  $\mathcal{M}_\bullet$ - $\sigma$  relation appears not to predict the nuclear star cluster masses below this limit. It is un-

likely that our surface brightness profile fitting code has overestimated the PS light by such large factors (§ 4), or that the  $M/L$  we adopted for the nuclear clusters is off by similar amounts. Some of the deviation may arise from the large intrinsic scatter in the  $\mathcal{M}_\bullet$ - $\sigma$  distribution in the low-mass range  $6 < \log(\mathcal{M}_\bullet) < 8$ ; see, e.g., Figure 7 from T02.

#### 5.4. Inner Profile Slopes

The *HST*-resolved, logarithmic slopes of inner surface brightness profiles are a useful galaxy parameter, as they can test the applicability of density profile models, which are often based on power laws (e.g., Jaffe 1983; Hernquist 1990; Dehnen 1993; Tremaine et al. 1994). Inner slopes constrain the shape of the potential and the types of orbits that may be present in the nuclei. On the observational side, interest in profile slopes arose from the discovery of a bimodal distribution of inner slopes in samples of intermediate- and high-luminosity elliptical galaxies (Ferrarese et al. 1994; L95; Gebhardt et al. 1996), which suggested different formation/evolution processes for the cores of giant and less luminous ellipticals, perhaps linked to the presence of binary black holes (e.g., F97).

For our galaxies, all surface brightness profiles continue to rise inward to the resolution limit of the data (Fig. 6). Inner profiles approximate power laws, although small but clear deviations are evident in Figure 6, making the slope determination dependent on the radial range used for the measurement. The presence of inner components further complicates matters and means that two types of profile slopes may be measured: the slope of the *total* surface brightness profile, or that of the underlying bulge component. Both have their own merits. The latter provides a cleaner measure

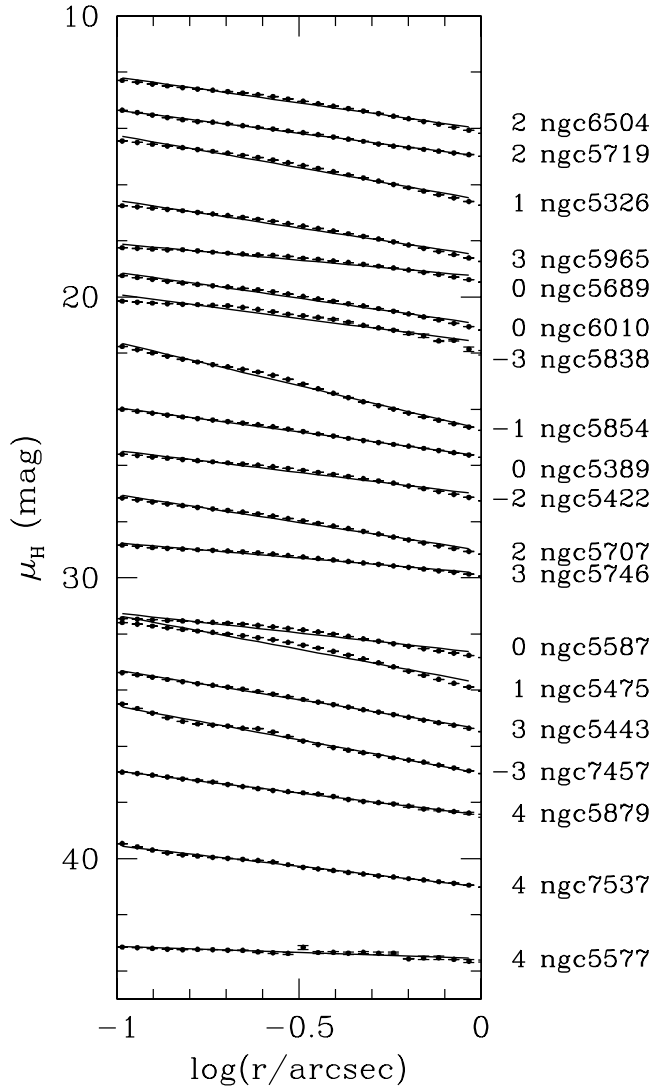


FIG. 6.—Inner surface brightness profiles plotted against  $\log R$  in the range  $0.1'' \leq R \leq 1''$  ( $R \equiv$  geometric mean radius). Profiles are sorted by decreasing bulge absolute magnitude, brightest above, and are offset by  $1.5 \text{ mag arcsec}^{-2}$  from each other for clarity. *Solid lines*: Direct least-squares power-law fits, with exponent  $\gamma$  given in Table 6, col. (2).

of the slope of the spheroidal component of the bulge, unaffected by inner disks/bars or point sources. To date, common practice has been to avoid such nuclear features when deriving the inner profile slope. On the other hand, a direct measure of the slope has the advantage of being independent of any model decomposition. Moreover, if the central SMBHs, known to reside in ellipticals and bulges (Kormendy & Richstone 1995), have grown adiabatically within the nuclear star clusters (e.g., Young 1980; van der Marel 1999), then the profile slope of the central cluster is of interest and should not be avoided—although resolution does become an issue.

Several methods have been employed in the past to measure the inner profile slope denoted by  $\gamma$ : a single power law (e.g., Phillips et al. 1996); a double power law (Ferrarese et al. 1994); a Nuker fit (L95); a measure of the logarithmic derivative of the best-fit Nuker law at either some fixed radius (usually denoted as  $\gamma'$ , e.g., in R01, and here denoted  $\gamma'_N$ ) or over some small interval, e.g.,  $0.1''$ – $0.5''$  (usually denoted as  $\langle\gamma\rangle$ ; e.g., Stiavelli et al. 2001); and the logarithmic derivative of the best-fit Sérsic model (de-

noted here as  $\gamma'_S$ ; Graham & Guzmán 2003). For the Sérsic model,  $\gamma'_S$  can easily be evaluated at any radius  $R$ , such that

$$\gamma'_S(R) \equiv \frac{-d \log I(R)}{d \log R} = \frac{b_n}{n} \left( \frac{R}{R_e} \right)^{1/n}, \quad (15)$$

where  $b_n \approx 1.9992n - 0.3271$ , and  $R_e$  is the effective radius.

For our sample, we have computed the inner profile slope following all of the methods outlined above, except for  $\langle\gamma\rangle$ , for lack of a precise definition of this quantity. The various determinations of the inner profile slopes are given in Table 6. These include direct power-law least-squares fits to the profiles over ranges of  $0.1'' < R < 1''$  and  $20 \text{ pc} < R < 200 \text{ pc}$ ,  $\gamma'_N(0.3'')$ ,  $\gamma'_S(0.3'')$ , and  $\gamma'_S(0.15R_e)$ . Comparison of the results indicates that direct power-law fits over ranges of  $0.1'' < R < 1''$  or  $20 \text{ pc} < R < 200 \text{ pc}$  yield slopes  $\gamma$  quite similar to  $\gamma'_N(0.3'')$  derived from a Nuker fit. Our Nuker fits extended inward to  $R = 0.1''$ ; hence, the similarity of  $\gamma(0.3'')$  to a direct power-law fit is not surprising: these three fits encompass any compact nuclear components. The values of  $\gamma'_S(0.3'')$  and  $\gamma'_S(0.15R_e)$ , which come from the Sérsic fits to the host bulge (§ 3), are equal to or lower than the other values. They provide the slope corresponding to the underlying bulge components, and, as such, they are the most directly comparable to the  $\langle\gamma\rangle$ -values presented by, e.g., Carollo & Stiavelli (1998) for late-type spirals, and those of Stiavelli et al. (2001) for dwarf ellipticals.

Figure 7 shows the  $B$ -band absolute magnitudes of the bulges plotted against the values of  $\gamma'_N$  derived at  $0.3''$ , and of  $\gamma'_S$  derived at  $R/R_e = 0.15$ . The  $B$ -band absolute magnitudes of the bulges were derived from the galaxy total corrected  $B$ -band magnitudes from the RC3 and the bulge-to-disk ratios derived in this paper; this procedure avoids  $B$ -band bulge-disk decompositions that are heavily affected by dust. Also included in the figure are the elliptical galaxy data from L95 (Nuker model  $\gamma$ ) and the dwarf elliptical data from Stiavelli et al. (2001; mean slope  $\langle\gamma\rangle$  between  $0.1''$  and  $0.5''$ ) and Graham & Guzmán (2003;  $\gamma'_S$  at  $R = 0.5''$  when the light of nuclear components is included (Fig. 7, *top*) and matches that of ellipticals of similar luminosities. When nuclear components are excluded (Fig. 7, *bottom*), slopes trace a continuous distribution in the range  $0 < \gamma < 1$ .

In a previous study of inner profile slopes of galaxy bulges, Carollo & Stiavelli (1998) obtained a range of  $0 < \gamma < 1$  values similar to us. However, they differ in the interpretation of the results. Because their distribution of  $\langle\gamma\rangle$  shows two distinct clumps, they argue that two separate families of bulges exist, i.e., “exponential” ( $\langle\gamma\rangle \sim 0.3$ ) and “ $R^{1/4}$ ” ( $\langle\gamma\rangle \sim 0.8$ ) bulges. Figure 7 shows that our bulges do not cluster in two clumps; instead, they cover a continuous range from the low to the high values of the Carollo & Stiavelli distribution. The origin for their bimodal distribution of  $\langle\gamma\rangle$  is unclear. Their  $\langle\gamma\rangle$ -values come from Nuker fits and not from exponential or  $R^{1/4}$  fits; hence, the bimodality should not be a consequence of their splitting the sample into exponential and  $R^{1/4}$  classes. But two aspects of their analysis could lead to a polarization of their  $\langle\gamma\rangle$  toward high and low values. One of these is the subjective choice of the radial range for the Nuker fits. While nuclear components are easy to identify by eye when the underlying profile is shallow, such as in an exponential bulge, for galaxies with steeper underlying bulge profiles ( $n \geq 2$ ), the “break” from the bulge to the nuclear component becomes weaker and easier to miss by eye; hence, the radial range occupied by the nuclear component can easily be included when performing the Nuker fit, yielding a biased, higher value of  $\langle\gamma\rangle$  than

TABLE 6  
INNER NEGATIVE LOGARITHMIC SLOPES

NGC (1)	$\gamma$ (pwl) (0.1''–1'') (2)	$\gamma$ (pwl) (20–200 pc) (3)	$\gamma'_N$ (0.3'') (4)	$\gamma'_S$ (0.3'') (5)	$\gamma'_S$ (0.15 $R_e$ ) (6)
5326.....	0.91	0.85	0.98	0.90	0.70
5389.....	0.69	0.70	0.72	0.43	0.39
5422.....	0.62	0.65	0.63	0.72	0.64
5443.....	0.83	0.83	0.84	0.59	0.72
5475.....	0.96	1.03	1.34	0.75	0.68
5577.....	0.17	0.22	0.16	0.30	0.22
5587.....	0.56	0.52	0.81	0.11	0.17
5689.....	0.46	0.43	0.49	0.18	0.17
5707.....	0.79	0.77	0.86	0.14	0.10
5719.....	0.66	0.65	0.67	0.70	0.42
5746.....	0.43	0.46	0.46	0.53	0.41
5838.....	0.67	0.84	0.78	0.47	0.26
5854.....	1.24	1.26	1.21	0.67	0.46
5879.....	0.63	0.67	0.65	0.79	0.76
5965.....	0.78	0.61	0.84	0.94	0.85
6010.....	0.74	0.77	0.76	0.75	0.75
6504.....	0.73	0.54	0.78	0.92	0.74
7457.....	0.96	0.97	0.92	1.12	0.82
7537.....	0.59	0.63	0.59	0.62	0.86

NOTES.—Col. (1): Galaxy NGC number. Col. (2):  $\gamma$  from power-law fit to 0.1''–1'' (Fig. 6). Col. (3):  $\gamma$  from power-law fit to 20–200 pc. Col. (4):  $\gamma'_N$ , slope of Nuker model at  $R = 0.3''$  (single Nuker fit to  $0.1'' < R \leq 4''$ ). Col. (5):  $\gamma'_S$ , slope of Sérsic model at  $R = 0.3''$  (simultaneous bulge, disk, and nuclear component fits). Col. (6):  $\gamma'_S$ , slope of Sérsic model at  $R/R_e = 0.15$ .

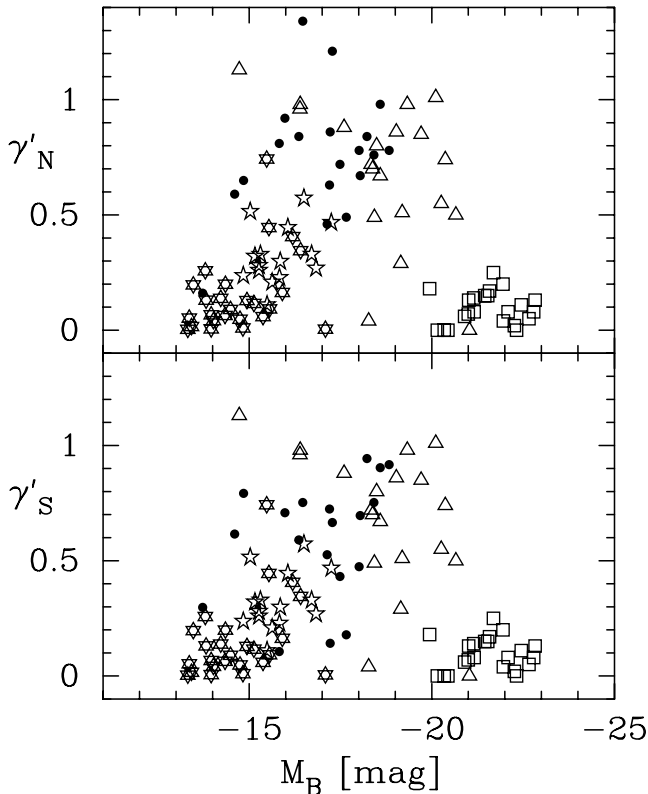


FIG. 7.—Spheroid  $B$ -band absolute magnitude plotted against two inner profile slope determinations,  $\gamma$ . *Top*: Slope  $\gamma'_N$  of the best-fit Nuker model at  $0.3''$ . *Bottom*: Slope  $\gamma'_S$  of the best-fit Sérsic profile at  $0.15R_e$ . *Filled circles*: Bulges; This work. *Squares*: Core ellipticals from L95. *Triangles*: Power-law ellipticals from L95. *Five-pointed stars*: Dwarf ellipticals from Graham & Guzmán (2003). *Six-pointed stars*: Dwarf ellipticals from Stiavelli et al. (2001).

that corresponding to the underlying bulge. Simultaneous fits to the bulge and the nuclear component are needed in those cases to remove such bias from the determination of the bulge profile slope. Another aspect that may polarize the  $\langle \gamma \rangle$  distribution into high and low clumps may be the derivation of bulge absolute magnitudes without a bulge-disk decomposition, and applying exponential- or  $R^{1/4}$ -constrained fits to profiles from small-field *HST* WFPC2 images:  $R^{1/4}$  models are known to overestimate the flux of  $R^{1/n}$  systems if  $n < 4$ , while exponential models are known to underestimate the flux in  $R^{1/n}$  systems that have  $n > 1$  (e.g., G01). Finally, sample selection may also be important. Their sample includes many barred galaxies and is overall of later type than ours, although we note that many of our bulges show exponential-like profiles, i.e., profiles that Carollo & Stiavelli associate with the low- $\langle \gamma \rangle$  clump. The above arguments, together with the distributions shown in Figure 7, suggest that the slopes of the total galaxy profiles (including nuclear components) cluster around  $0.5 < \gamma < 1$ , but bulge profiles as a class cover a continuous distribution of nuclear slopes in the range  $0 < \gamma < 1$ .

## 6. CONCLUSIONS

At *HST* resolution, nuclear photometric components, in addition to the Sérsic bulge and the exponential outer disk, are exceedingly common ( $\sim 90\%$ ) in early- to intermediate-type disk galaxies. Spatially resolved nuclear components are found in 58% of our sample. These components are geometrically flat systems and could be disks, bars, or rings. The ones detected have a central surface brightness comparable to the underlying bulges, but fainter such systems may exist. The isophotal signatures indicate total sizes of a few hundred parsecs, similar to those of inner bars in double-barred galaxies. Often, such components are reddened by dust; the evidence from optical and NIR colors, presented in Paper I, as well as their high densities, suggest that they are old rather than late additions to the bulges.

A majority of the galaxies ( $\sim 58\%$ ) harbor sources unresolved by *HST* NICMOS2. They are most likely star clusters, with

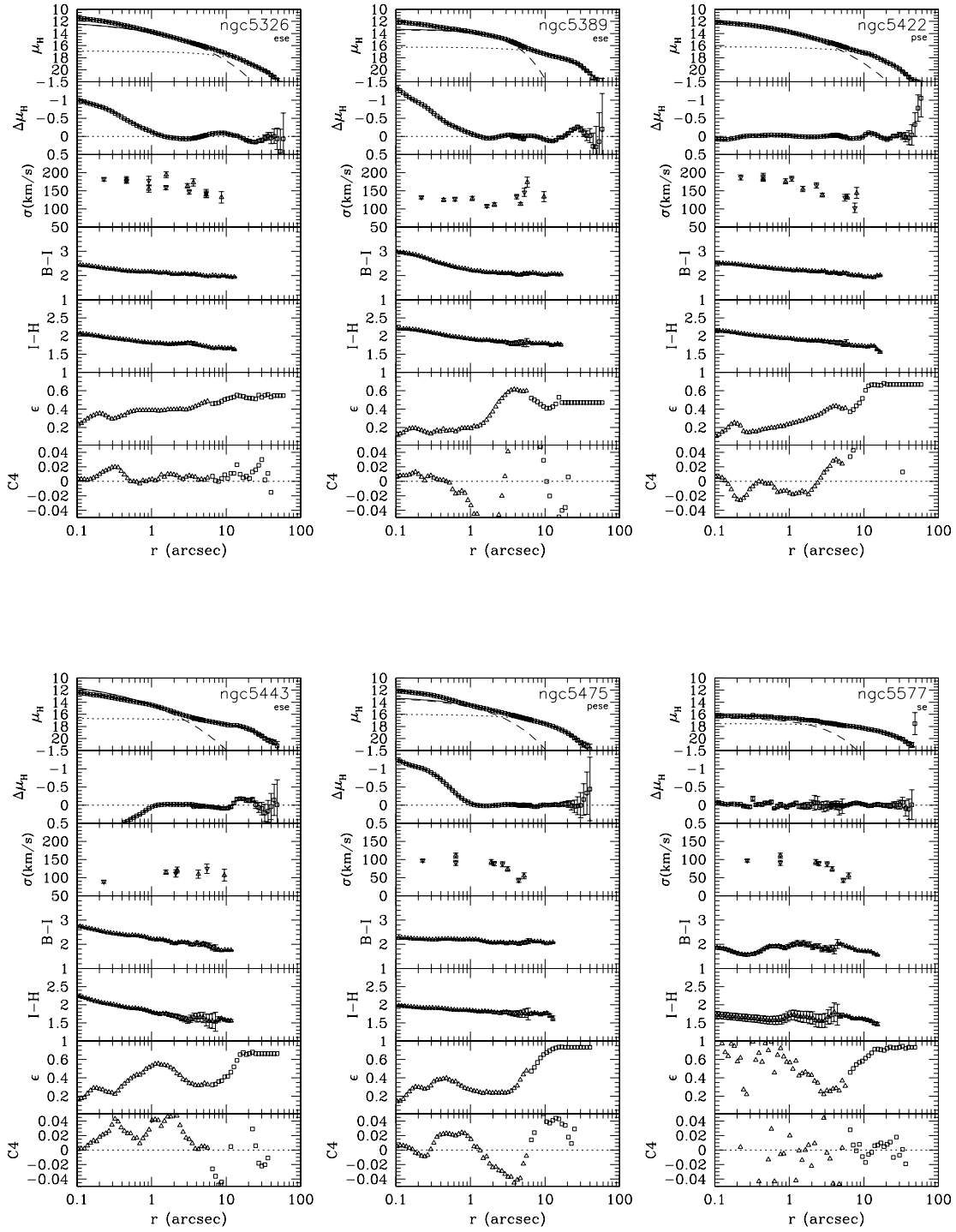


FIG. 8.—Profiles of surface brightness, velocity dispersion,  $B - I$ ,  $I - H$ , ellipticity, and  $c4$  diskiness/boxiness coefficient. The abscissa is the logarithm of the geometric mean axis in arcseconds.  $\mu_H$ : Combined  $HST+GB$  surface brightness profile, and model fits excluding the central arcsecond (*dashed line*: Sérsic bulge; *dotted line*: exponential disk).  $\Delta\mu_H$ : Residuals from the fit (data minus model).  $\sigma$ : Minor-axis velocity dispersion profiles from Falcón-Barroso et al. (2003), folded around the origin (*triangles*: dust-free side; *inverted triangles*: side seen through the disk; the abscissa has been projected to the geometric mean radius using the mean of the ellipticity profile; the central velocity dispersion measurement has been plotted at  $r = 0.18''$ , corresponding to 1 half-pixel of the spectrograph).  $B - I$ ,  $I - H$ : Minor-axis color profiles for the dust-free side of the bulge, derived from combined  $HST+GB$  profiles, from Paper I. The abscissa has been projected to the geometric mean radius using the ellipticity profiles.  $\epsilon$ : Triangles are the ellipticity profile from ellipse fits to the  $HST$  NICMOS F160W images; squares are the  $\epsilon$  profile from ellipse fits to GB  $K$ -band images, from Peletier & Balcells (1997); GB  $\epsilon$  values are generally kept fixed in the outer, low-S/N region of the images.  $c4$ : Fourth-order cosine term of the residuals from ellipse fits (*triangles*:  $HST$  F160W images; *squares*: GB  $K$ -band images).

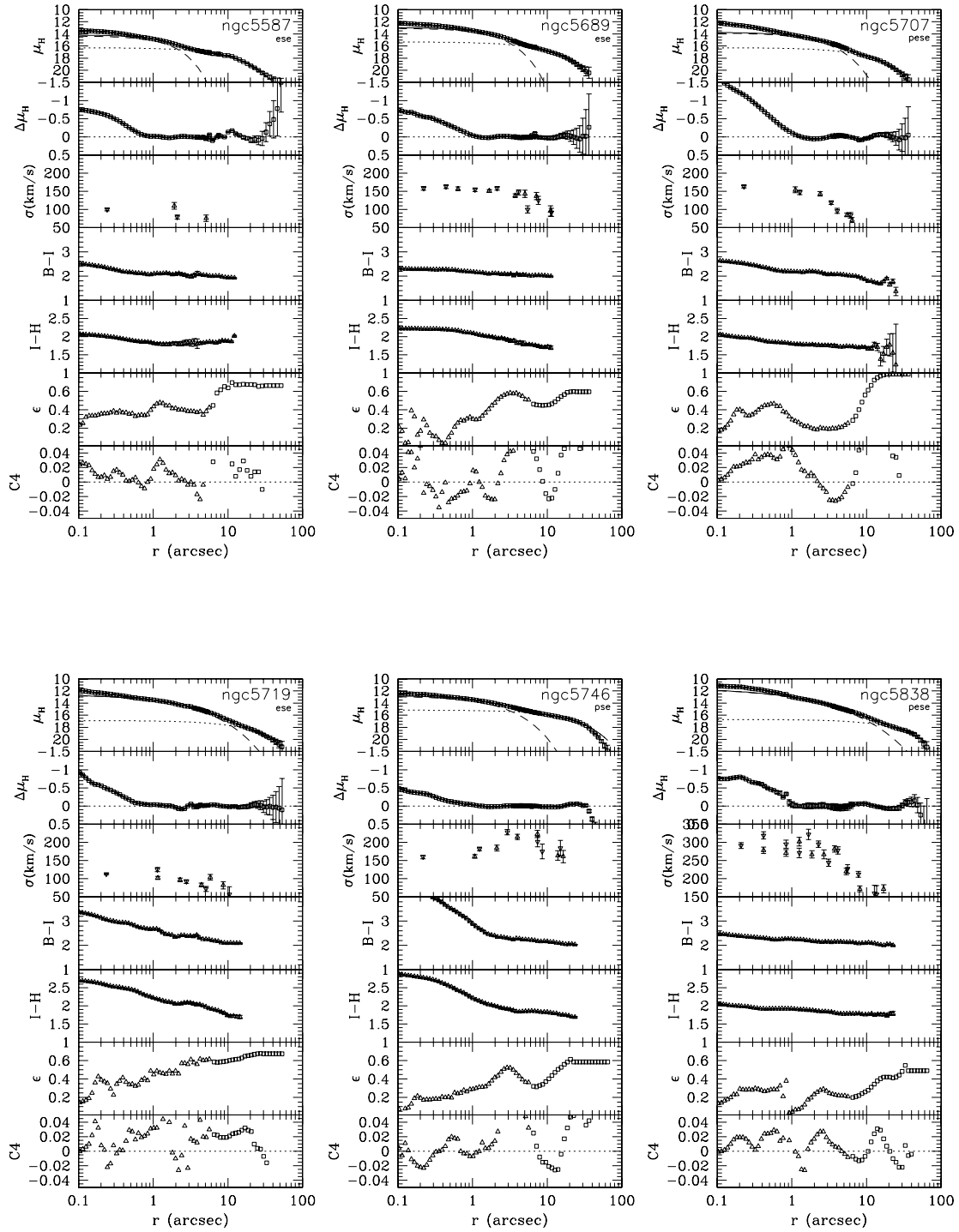


FIG. 8— *Continued*

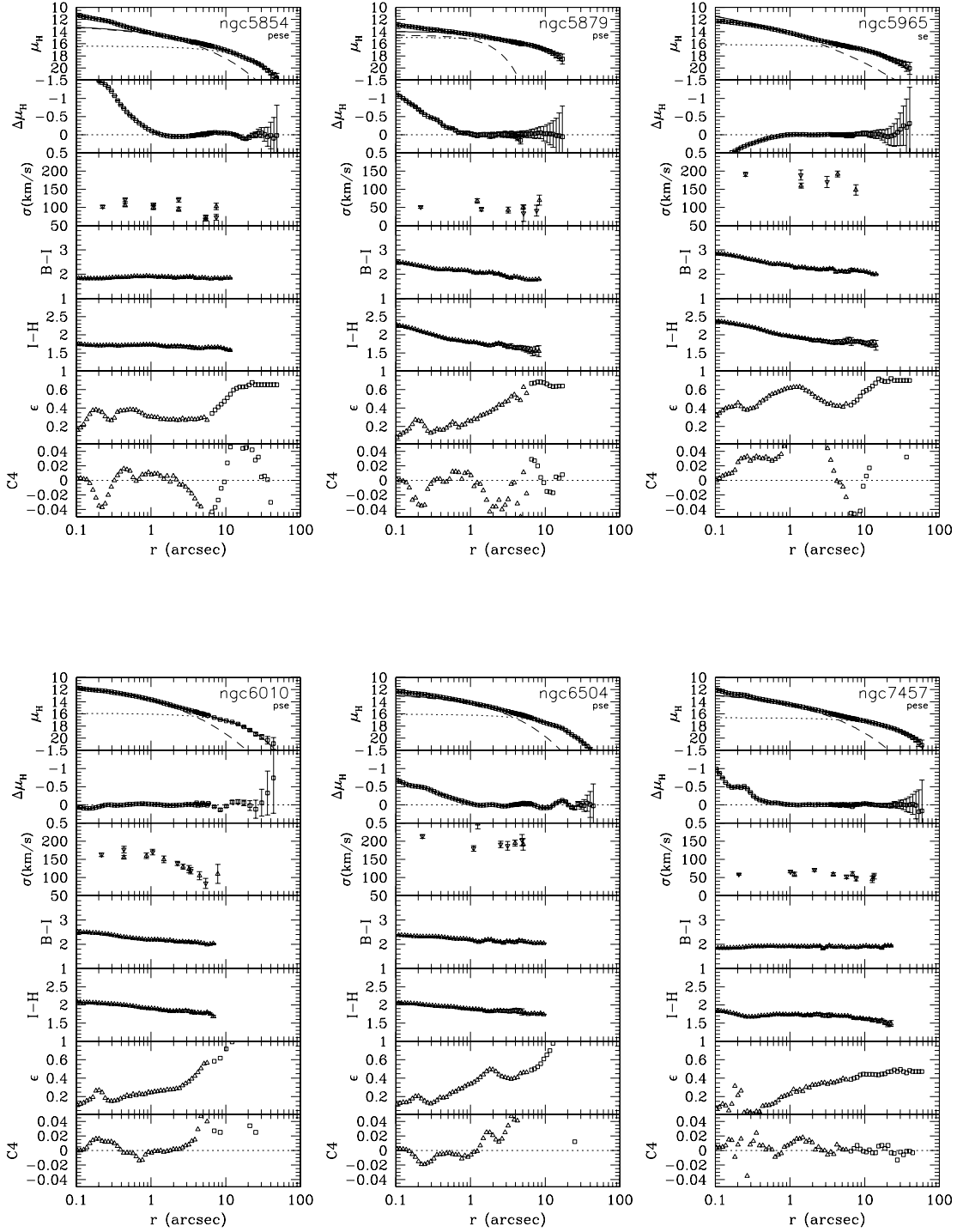
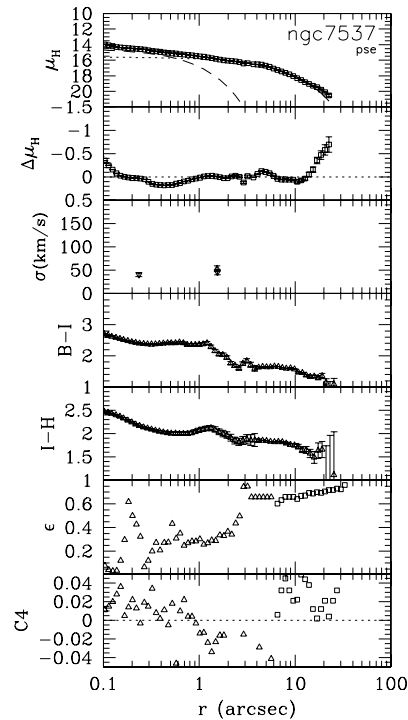


FIG. 8—Continued

luminosities corresponding to 10–20 globular clusters, and similar to other unresolved sources found in the nuclei of ellipticals, dwarf ellipticals, and bulges. When combined with similar nuclear components in dE galaxies, their photometric masses scale with spheroidal mass as  $M_{\text{PS}}/M_{\odot} = 10^{7.73 \pm 0.16} (M_{\text{bul}}/10^{10} M_{\odot})^{0.76 \pm 0.13}$ . Our central star clusters fall above the faintward extrapolation of  $M_{\bullet}$ - $M_{\text{bul}}$  relations derived by HR04 or F06. In order to extend a CMO-style relation to faint spheroidal luminosities, a moderate nonlinearity is needed, and we propose the relation  $M_{\text{CMO}}/M_{\odot} = 10^{7.51 \pm 0.06} (M_{\text{bul}}/10^{10} M_{\odot})^{0.84 \pm 0.06}$ . But we see additional difficulties with the CMO picture in that all of our PSs show masses

above the cluster–black hole transitional mass of  $10^7 M_{\odot}$  proposed by Wehner & Harris (2006).

Bulge surface brightness profiles rise inward to the limit of the *HST* NICMOS resolution,  $\sim 10$  pc for the current sample. While the inner bulge profiles deviate from pure power laws, “break radii” in a Nuker law sense are not present. Structurally, the bulges of early- to intermediate-type galaxies may be globally grouped with the “power-law” intermediate- and low-luminosity elliptical galaxies. Negative logarithmic nuclear profile slopes of the Sérsic bulge components,  $\gamma$ , cover a continuous range of  $0 < \gamma < 1$ , overlapping with dwarf ellipticals at the faint end and with

FIG. 8— *Continued*

intermediate-luminosity ellipticals at the bright end. We find no evidence to support a bimodal distribution of  $\gamma$  reported by others.

This research has made use of the NASA/IPAC Extragalactic Database (NED), which is operated by the Jet Propulsion Labo-

ratory, California Institute of Technology, under contract with the National Aeronautics and Space Administration. This research has made use of the HyperLeda database. The United Kingdom Infrared Telescope is operated by the Joint Astronomy Centre on behalf of the UK Particle Physics and Astronomy Research Council.

## APPENDIX

### SURFACE BRIGHTNESS, ISOPHOTAL, DYNAMICAL, AND COLOR PROFILES

Figure 8 shows the surface brightness profiles together with dynamical, isophotal, and color profiles for each galaxy. The top panels show the combined *HST*+*GB*  $\mu_H$  profile, and Sérsic+exponential fit carried out excluding the inner  $1''$ . Beneath the galaxy name is the fit type code corresponding to the full fit, including additional nuclear components, from Table 2. The second panels give the residuals from the fit. The third panels show the minor-axis velocity dispersion profiles, folded around the origin, from Falcón-Barroso et al. (2003); the abscissa has been scaled to the geometric mean radius using the mean of the ellipticity profile. The fourth and fifth panels show the combined *HST*+*GB* minor-axis  $B - I$  and  $I - H$  color profiles on the side of the bulge not seen through the disk (the “dust-free” side), from Paper I; the abscissa has been scaled to the geometric mean radius using the mean of the ellipticity profile. The sixth panels show the ellipticity profile, and the bottom panels show the fourth-order Fourier cosine term,  $c_4$ , from the ellipse fits; inside  $6''$  (*triangles*) the latter two profiles are derived from *HST* NICMOS F160W images, while outside  $6''$  (*squares*) they are derived from the UKIRT *K*-band images (Peletier & Balcells 1997).

## REFERENCES

- Aaronson, M. 1978, *PASP*, 90, 28  
Aguerri, J. A. L., Balcells, M., & Peletier, R. F. 2001, *A&A*, 367, 428  
Allen, C. W. 1973, *Astrophysical Quantities* (3rd ed.; London: Athlone)  
Andredakis, Y. C., Peletier, R. F., & Balcells, M. 1995, *MNRAS*, 275, 874 (APB95)  
Andredakis, Y. C., & Sanders, R. H. 1994, 1994, *MNRAS*, 267, 283  
Athanasoula, E. 2005, *MNRAS*, 358, 1477  
Balcells, M., Graham, A. W., Domínguez-Palmero, L., & Peletier, R. F. 2003, *ApJ*, 582, L79 (Paper II)  
Balcells, M., Graham, A. W., & Peletier, R. F. 2007, *ApJ*, 665, 1104 (Paper IV)  
Balcells, M., & Peletier, R. F. 1994, *AJ*, 107, 135 (BP94)  
Bell, E. F., & de Jong, R. S. 2001, *ApJ*, 550, 212  
Binggeli, B., Sandage, A., & Tarenghi, M. 1984, *AJ*, 89, 64  
Böker, T., Laine, S., van der Marel, R. P., Sarzi, M., Rix, H. W., Ho, L. C., & Shields, J. C. 2002, *AJ*, 123, 1389  
Bouwens, R., Cayón, L., & Silk, J. 1999, *ApJ*, 516, 77  
Bureau, M., Aronica, G., Athanassoula, E., Dettmar, R.-J., Bosma, A., & Freeman, K. C. 2006, *MNRAS*, 370, 753  
Bureau, M., & Freeman, K. C. 1999, *AJ*, 118, 126  
Caldwell, N., & Bothun, G. D. 1987, *AJ*, 94, 1126  
Caon, N., Capaccioli, M., & D’Onofrio, M. 1993, *MNRAS*, 265, 1013  
Carollo, C. M. 1999, *ApJ*, 523, 566  
Carollo, C. M., & Stiavelli, M. 1998, *AJ*, 115, 2306  
Carollo, C. M., Stiavelli, M., de Zeeuw, P. T., & Mack, J. 1997, *AJ*, 114, 2366  
Carollo, C. M., Stiavelli, M., de Zeeuw, P. T., Seigar, M., & Dejonghe, H. 2001, *ApJ*, 546, 216  
Carollo, C. M., Stiavelli, M., & Mack, J. 1998, *AJ*, 116, 68  
Carollo, C. M., Stiavelli, M., Seigar, M., de Zeeuw, P. T., & Dejonghe, H. 2002, *AJ*, 123, 159  
Castro-Rodríguez, N., & Garzón, F. 2003, *A&A*, 411, 55

- Combes, F., Debbasch, F., Friedli, D., & Pfenniger, D. 1990, *A&A*, 233, 82  
 Côté, P., et al. 2006, *ApJS*, 165, 57  
 Dehnen, W. 1993, *MNRAS*, 265, 250  
 de Jong, R. S. 1996, *A&A*, 313, 45  
 de Vaucouleurs, G., de Vaucouleurs, A., Corwin, H. G., Buta, R. J., Paturel, G., & Fouque, P. 1991, *Third Reference Catalogue of Bright Galaxies* (Berlin: Springer) (RC3)  
 Erwin, P. 2004, *A&A*, 415, 941  
 Erwin, P., & Sparke, L. S. 2002, *AJ*, 124, 65  
 Eskridge, P. B., et al. 2002, *ApJS*, 143, 73  
 Faber, S. M., et al. 1997, *AJ*, 114, 1771 (F97)  
 Falcón-Barroso, J., Balcells, M., Peletier, R. F., & Vazdekis, A. 2003, *A&A*, 405, 455  
 Falcón-Barroso, J., Peletier, R. F., & Balcells, M. 2002, *MNRAS*, 335, 741  
 Falcón-Barroso, J., et al. 2006, *MNRAS*, 369, 529  
 Ferrarese, L., van den Bosch, F. C., Ford, H. C., Jaffe, W., & O'Connell, R. W. 1994, *AJ*, 108, 1598  
 Ferrarese, L., et al. 2006, *ApJS*, 164, 334 (F06)  
 Gebhardt, K., et al. 1996, *AJ*, 112, 105  
 Graham, A. W. 2001a, *AJ*, 121, 820 (G01)  
 ———. 2001b, *MNRAS*, 326, 543  
 ———. 2002, *MNRAS*, 334, 721  
 Graham, A. W., & de Blok, W. J. G. 2001, *ApJ*, 556, 177  
 Graham, A. W., & Driver, S. P. 2005, *Publ. Astron. Soc. Australia*, 22, 118  
 Graham, A. W., Erwin, P., Caon, N., & Trujillo, I. 2001a, *ApJ*, 563, L11  
 Graham, A. W., & Guzmán, R. 2003, *AJ*, 125, 2936  
 Graham, A. W., Trujillo, I., & Caon, N. 2001b, *AJ*, 122, 1707  
 Häring, N., & Rix, H.-W. 2004, *ApJ*, 604, L89 (HR04)  
 Hernquist, L. 1990, *ApJ*, 356, 359  
 Holfeltz, S. T., & Calzetti, D. 1999, *Instrument Sci. Rep. NICMOS-99-007* (Baltimore: STScI), [http://www.stsci.edu/hst/nicmos/documents/isrs/isr\\_99\\_007.pdf](http://www.stsci.edu/hst/nicmos/documents/isrs/isr_99_007.pdf)  
 Jaffe, W. 1983, *MNRAS*, 202, 995  
 Jørgensen, I., Franx, M., & Kjaergaard, P. 1992, *A&AS*, 95, 489  
 Kauffmann, G., Charlot, S., & White, S. D. M. 1996, *MNRAS*, 283, L117  
 Kent, S. M., Dame, T. M., & Fazio, G. 1991, *ApJ*, 378, 131  
 Khosroshahi, H. G., Wadadekar, Y., & Kembhavi, A. 2000, *ApJ*, 533, 162  
 Knapen, J. H., Beckman, J. E., Shlosman, I., Peletier, R. F., Heller, C. H., & de Jong, R. S. 1995, *ApJ*, 443, L73  
 Kormendy, J. 1985, *ApJ*, 295, 73  
 Kormendy, J., & Kennicutt, R. C., Jr. 2004, *ARA&A*, 42, 603  
 Kormendy, J., & Richstone, D. 1995, *ARA&A*, 33, 581  
 Kuijken, K., & Merrifield, M. R. 1995, *ApJ*, 443, L13  
 Laor, A. 2001, *ApJ*, 553, 677  
 Lauer, T. R., et al. 1995, *AJ*, 110, 2622 (L95)  
 Laurikainen, E., Salo, H., & Buta, R. 2005, *MNRAS*, 362, 1319  
 Leitherer, C., et al. 1996, *PASP*, 108, 996  
 MacArthur, L. A., Courteau, S., & Holtzman, J. A. 2003, *ApJ*, 582, 689  
 McDermid, R. M., et al. 2006, *MNRAS*, 373, 906  
 McLaughlin, D. E., King, A. R., & Nayakshin, S. 2006, *ApJ*, 650, L37  
 Merritt, D., & Ferrarese, L. 2001, *ApJ*, 547, 140  
 Möllenhoff, C., & Heidt, J. 2001, *A&A*, 368, 16  
 Nilson, P. 1973, *Uppsala General Catalogue of Galaxies* (Uppsala: Astronomiska Obs.)  
 Peletier, R. F., & Balcells, M. 1996, *AJ*, 111, 2238  
 ———. 1997, *NewA*, 1, 349  
 Peletier, R. F., Balcells, M., Davies, R. L., Andredakis, Y., Vazdekis, A., Burkert, A., & Prada, F. 1999, *MNRAS*, 310, 703 (Paper I)  
 Pfenniger, D. 1993, in *IAU Symp. 153, Galactic Bulges*, ed. H. Dejonghe & H. J. Habing (Dordrecht: Kluwer), 387  
 Pfenniger, D., & Norman, C. 1990, *ApJ*, 363, 391  
 Phillips, A. C., Illingworth, G. D., MacKenty, J. W., & Franx, M. 1996, *AJ*, 111, 1566  
 Ravindranath, S., Ho, L. C., Peng, C. Y., Filippenko, A. V., & Sargent, W. L. W. 2001, *AJ*, 122, 653  
 Renzini, A. 1999, in *The Formation of Galactic Bulges*, ed. C. M. Carollo, H. C. Ferguson, & R. F. G. Wyse (Cambridge: Cambridge Univ. Press), 9  
 Rest, A., van den Bosch, F. C., Jaffe, W., Tran, H., Tsvetanov, Z., Ford, H. C., Davies, J., & Schafer, J. 2001, *AJ*, 121, 2431 (R01)  
 Rieke, G. H., & Lebofsky, M. J. 1985, *ApJ*, 288, 618  
 Rossa, J., van der Marel, R. P., Böker, T., Gerssen, J., Ho, L. C., Rix, H.-W., Shields, J. C., & Walcher, C.-J. 2006, *AJ*, 132, 1074  
 Scannapieco, C., & Tissera, P. B. 2003, *MNRAS*, 338, 880  
 Scorza, C., & Bender, R. 1995, *A&A*, 293, 20  
 Scorza, C., & van den Bosch, F. C. 1998, *MNRAS*, 300, 469  
 Seigar, M., Carollo, C. M., Stiavelli, M., de Zeeuw, P. T., & Dejonghe, H. 2002, *AJ*, 123, 184  
 Seigar, M. S., & James, P. A. 1998, *MNRAS*, 299, 672  
 Sérsic, J. L. 1963, *Boletín de la Asociación Argentina de Astronomía*, 6, 41  
 Seth, A. C., Dalcanton, J. J., Hodge, P. W., & Debattista, V. P. 2006, *AJ*, 132, 2539  
 Silk, J. 2005, *MNRAS*, 364, 1337  
 Sommer-Larsen, J., Götz, M., & Portinari, L. 2003, *ApJ*, 596, 47  
 Stiavelli, M., Miller, B. W., Ferguson, H. C., Mack, J., Whitmore, B. C., & Lotz, J. M. 2001, *AJ*, 121, 1385  
 Tremaine, S., Richstone, D. O., Byun, Y., Dressler, A., Faber, S. M., Grillmair, C., Kormendy, J., & Lauer, T. R. 1994, *AJ*, 107, 634  
 Tremaine, S., et al. 2002, *ApJ*, 574, 740 (T02)  
 Trujillo, I., Graham, A. W., & Caon, N. 2001, *MNRAS*, 326, 869  
 van der Marel, R. P. 1999, *AJ*, 117, 744  
 Vazdekis, A., Casuso, E., Peletier, R. F., & Beckman, J. E. 1996, *ApJS*, 106, 307  
 Walcher, C. J., Böker, T., Charlot, S., Ho, L. C., Rix, H.-W., Rossa, J., Shields, J. C., & van der Marel, R. P. 2006, *ApJ*, 649, 692  
 Wehner, E. H., & Harris, W. E. 2006, *ApJ*, 644, L17  
 Wyse, R. F. G., Gilmore, G., & Franx, M. 1997, *ARA&A*, 35, 637  
 Young, P. 1980, *ApJ*, 242, 1232  
 Zhang, X. 1999, *ApJ*, 518, 613  
 Zoccali, M., et al. 2003, *A&A*, 399, 931